EES Catalysis

REVIEW ARTICLE

View Article Online
View Journal | View Issue

Cite this: *EES Catal.*, 2023, 1, 369

Layered double hydroxides and their composites as high-performance photocatalysts for CO_2 reduction

Guixiang Ding,†[a] Chunxue Li,†[b] Yonghao Ni,[c] Lihui Chen,[a] Li Shuai[a] and Guangfu Liao *[a]

Received 11th April 2023,
Accepted 27th April 2023

DOI: 10.1039/d3ey00080j

rsc.li/eescatalysis

Over the past decade, layered double hydroxides (LDHs) have attracted much attention due to their many advantages in the field of CO_2 photoreduction, such as superior CO_2 adsorption and tunable photoelectrochemical properties. Moreover, their low price, simple production process and high yield make it easier to realize mass production. This review presents a panorama of the latest developments of LDH-based photocatalysts for CO_2 reduction. It starts with the basic principle of photocatalytic CO_2 reduction. After that, the fundamentals of LDHs are also illustrated. Later, a series of representative LDH-based photocatalysts (mainly including LDH-based derivatives and LDH composites) for CO_2 reduction are exemplified. At the end, this review also offers some new views into the major challenges, opportunities, and heuristic perspectives for future research in this emerging field. There is no doubt that the advanced LDH-based materials can act as highly efficient photocatalysts to achieve new breakthroughs in CO_2 photoreduction.

Broader context

Photocatalytic CO_2 reduction technology is inspired by artificial photosynthesis, in which using a semiconductor to capture solar energy is considered as a promising strategy because of its advantages of zero energy consumption, low cost, and low toxicity. Layered double hydroxides (LDHs) have attracted much attention due to their many advantages in the field of CO_2 photoreduction, such as superior CO_2 adsorption, tunable photoelectrochemical properties and low-cost characteristic. This review presents a panorama of the latest developments of LDH-based photocatalysts for CO_2 reduction. It starts with the basic principle of photocatalytic CO_2 reduction. After that, the fundamentals of LDHs are also illustrated. Later, a series of representative LDH-based photocatalysts (mainly including derivative LDHs and LDH composites) for CO_2 reduction are exemplified. At the end, this review also offers some new views into the major challenges, opportunities, and heuristic perspectives for future research in this emerging field.

1. Introduction

With the industrialization development of human society, the demand for energy is also increasing day by day.[1–7] And the continued energy consumption depends mainly on the limited non-renewable fossil energy sources (coal, oil and natural gas).[8–13] As we know, the emission of CO_2 produced by burning fossil fuels is the chief culprit leading to global warming.[14–18] Therefore, it has become a hot topic in the field of science to reduce the greenhouse effect and excessive energy consumption by converting CO_2 into high value-added chemicals (*e.g.*, CH_3OH, CO, CH_4, HCOOH, *etc.*).[19,20] Recently, strategies that have been applied in converting CO_2 into fuel include electrocatalysis, chemical reformation, biochemical transformation, and hydrogenation, as well as thermal catalysis and photocatalytic methods.[21,22] Among them, photocatalytic CO_2 reduction technology is inspired by artificial photosynthesis, in which using a semiconductor to capture solar energy is considered as a promising strategy because of its advantages of zero energy consumption, low cost, and low toxicity.[23–30]

The phenomenon of photocatalysis was discovered by Honda-Fujishima in the 1970s, where semiconductor TiO_2 initiated the decomposition of water under the condition of light radiation.[31,32] Subsequently, the photocatalytic mechanism was studied based on the TiO_2 platform, and other photocatalytic materials were also developed.[16,33–36] As the earliest photocatalyst, TiO_2 owns a wide band gap

[a] College of Materials Engineering, Fujian Agriculture and Forestry University, Fuzhou 350002, China. E-mail: liaogf@mail2.sysu.edu.cn
[b] College of Ecological Environment and Urban Construction, Fujian University of Technology, Fuzhou 350118, China
[c] Limerick Pulp and Paper Centre, Department of Chemical Engineering, University of New Brunswick, Fredericton, New Brunswick E3B5A3, Canada
† These authors contributed equally to this work.

(~3.2 eV *vs. NHE*).[37–40] However, the wavelength range of visible light is from 400 nm to 760 nm, which means that TiO_2 exhibits photocatalytic properties only when driven by ultraviolet (UV) light with high energy.[41–44] Meanwhile, the disadvantages inherent to TiO_2 such as the rapid recombination of photogenerated carriers and the poor adsorption capacity are also obstacles to the improvement of the photocatalytic performance.[39,45–47] Therefore, it has become a mainstream development trend to optimize this material or to explore other outstanding materials for photocatalytic application in the field of photocatalysis.[48,49]

In view of the above description, advanced photocatalytic materials are the basic demands of photocatalytic CO_2 reduction.[50–52] Presently, the common semiconductors known to be developed can be roughly divided into oxide (WO_3, ZnO, TiO_2, Fe_2O_3, Co_xO_y, *etc.*), sulfide (CdS, MoS_2, $ZnIn_2S_4$, *etc.*), perovskite ($BaTiO_3$, $SrTiO_3$, *etc.*), nitrogen and carbon compounds (g-C_3N_4, SiC, B_4C, *etc.*), and so on.[49,53–58] Among the various semiconductors, layered double hydroxides (LDHs) have gained extensive attention, owning to their specific lamellar structure, compositionally tunable structures, and optical properties.[59–67] These features endow LDH materials with better CO_2 adsorption capacity and optional active sites. Thus, it is absolutely essential to deepen the research and application of LDH-based materials in the field of photocatalytic CO_2 reduction.[68,69]

In this review, we provide a panorama of the latest developments of LDH-based photocatalysts for CO_2 reduction. It starts with the basic principle of photocatalytic CO_2 reduction. After that, the fundamentals of LDHs are also illustrated. Later, a series of representative LDH-based photocatalysts (mainly including LDH-based derivatives and LDH composites) for CO_2 reduction are exemplified. At the end, this review also offers some new views into the major challenges, opportunities, and heuristic perspectives for future research in this emerging field. There is no doubt that the advanced LDH-based materials can act as highly efficient photocatalysts to achieve new breakthroughs in CO_2 photoreduction.

2. The fundamentals for CO_2 photoreduction

2.1. Mechanism and process for photocatalytic CO_2 reduction

The majority of materials used in photocatalysis are semiconductors and semiconductor-like materials; thus, energy band theory plays an irreplaceable role in understanding photocatalytic procedures.[15,70–72] The formation of the energy band is realized by the interaction between atoms.[73–76] When atoms are close to each other, the original energy levels of the atoms split into a group of energy levels with small energy difference.[77–82] Such a group of energy levels is called the energy band (Fig. 1). Because the energy difference of the energy levels in the a-band is very small, it can be regarded as continuous, and there is a zone without energy levels between the a-band and the b-band, which is called the band gap (E_g).[83–86] When the atom is in the

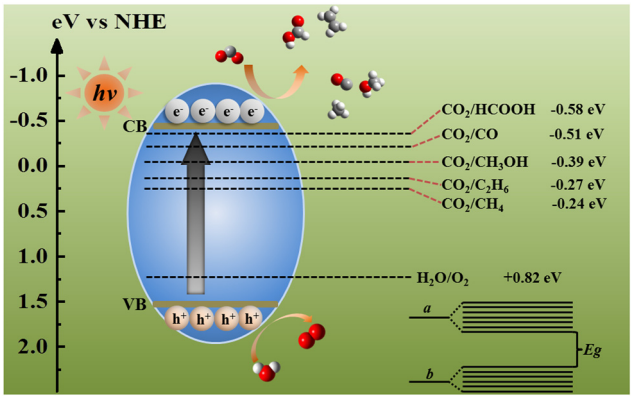

Fig. 1 The fundamentals of photocatalytic CO_2 reduction.

unexcited state, the electrons in the atom are arranged from the low-energy level to the high-energy level in turn, and the energy level filled with electrons is called the filled band. For the filled band, the energy level with the highest energy and closest to the empty energy band is denoted the valence band (VB), and the band that is not filled with electrons is the conduction band (CB).[87,88] VB electrons driven by light energy remain in the CB and cross E_g, so the excited electron transition leads to the differentiation of positive and negative charges in semiconductors. Excited electrons are called photogenerated electrons (e^-).[89,90] After the transition, the VB loses negative charges and shows positive charges, which are called holes (h^+).[91] From a thermodynamic viewpoint, these e^-–h^+ pairs can cause the surface reduction and oxidation reactions only if their respective reduction and oxidation potentials are located between the CB and VB potentials. The standard redox potentials for CO_2 reduction (Table 1) indicate that multi-electron reduction reactions are more conducive to the surface-active sites of semiconductors.

Photocatalytic reaction is the combination of photoreaction and catalytic reaction, which is driven by light energy to promote the photocatalyst to convert reactants into products. Chlorophyll, a natural photocatalyst in plants, is the earliest photocatalyst that human beings came into contact with. The reason why the photocatalyst has catalytic ability under illumination is that when sunlight is irradiated on the photocatalyst surface, it produces reductive e^- and oxidizing h^+.[39,94–99] For

Table 1 Standard redox potentials for CO_2 photoreduction[92,93]

Reaction	E^0 (V) *vs.* NHE at pH = 7
CO_2 (g) + e^- → $CO_2^{\bullet-}$	−1.9
CO_2 (g) + $2H^+$ + $2e^-$ → HCOOH (aq)	−0.61
CO_2 (g) + $2H^+$ + $2e^-$ → CO (g) + H_2O (aq)	−0.53
CO_2 (g) + $4H^+$ + $4e^-$ → HCHO (aq) + H_2O (aq)	−0.48
CO_2 (g) + $6H^+$ + $6e^-$ → CH_3OH (aq) + H_2O (aq)	−0.38
CO_2 (g) + $8H^+$ + $8e^-$ → CH_4 (aq) + $2H_2O$ (aq)	−0.24
$2CO_2$ (g) + $6H_2O$ (aq) + $10e^-$ → C_2H_2 (q) + $10OH^-$	−0.362
$2CO_2$ (g) + $8H_2O$ (aq) + $12e^-$ → C_2H_4 (q) + $12OH^-$	−0.349
$2CO_2$ (g) + $9H_2O$ (aq) + $12e^-$ → C_2H_5OH (aq) + $12OH^-$	−0.329
$2CO_2$ (g) + $13H_2O$ (aq) + $18e^-$ → C_3H_7OH (aq) + $18OH^-$	−0.31

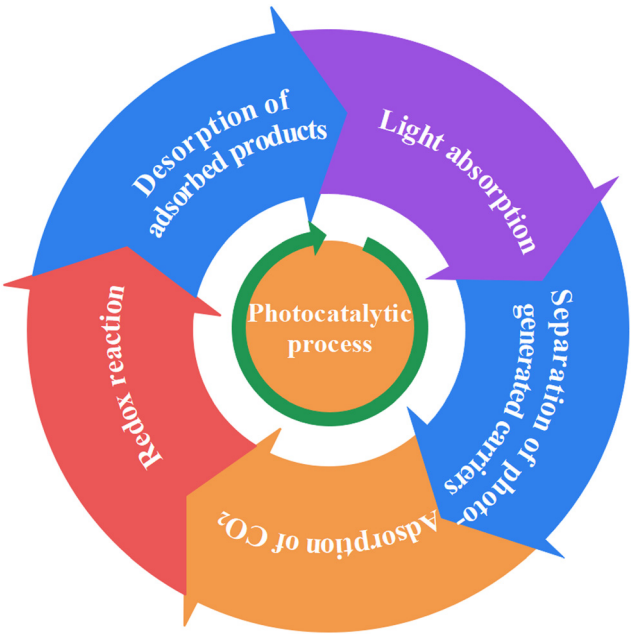

Fig. 2 The photocatalytic process of CO_2 reduction.

photocatalytic CO_2 reduction, CO_2 combines with e^-, chemisorption occurs and then it is further reduced to the target products (Fig. 1). Therefore, the photocatalytic process can be divided into the following 5 processes (Fig. 2),[100,101] namely (i) light absorption, (ii) separation of photo-generated carriers, (iii) adsorption of CO_2, (iv) redox reaction, and (v) desorption of adsorbed products. The overall photocatalysis efficiency is strongly dependent on the cumulative effect of these four consecutive steps, which can be expressed as below: $\eta_c = \eta_{abs} \times \eta_{cs} \times \eta_{cmt} \times \eta_{cu}$, where η_c, η_{abs}, η_{cs}, η_{cmt}, and η_{cu} represent the photonic conversion, photon absorption, charge excitation/separation, charge migration/transport, and charge utilization efficiencies, respectively.[102,103] The kinetic obstacles can be summarized as below: (i) the photocatalyst surface morphology affects photon absorption, (ii) the quick recombination kinetics of e^-–h^+ pairs is one of the most challenging obstacles, (iii) the low specific surface area and significant agglomeration of a nanostructured photocatalyst greatly decrease the surface redox kinetics and increase the diffusion barriers of the reagent, and (iv) as an uphill reaction, CO_2 photoreduction, with its slow surface multi-electron reaction, results in the accumulation of photogenerated e^- and h^+ and thus, e^-–h^+ recombination and photocorrosion that consequently reduce their photocatalytic activity. Therefore, the kinetic factors are considered to be more important than the thermodynamic factors for the design and development of high-performance CO_2 photoreduction catalysts.

2.2. The structure and application of LDHs

Layered double hydroxides (LDHs), also known as hydrotalcite-like compounds, are a group of 2D original existing and/or artificially synthesized anionic clay materials.[104,105] These materials were exposed in Sweden in about 1842, but it was not until

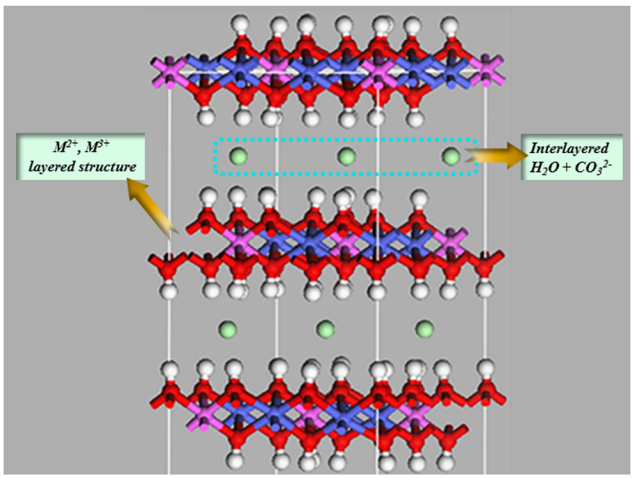

Fig. 3 The detailed structure of LDHs.

1915 that Manasse reported the precise formula of the natural mineral hydrotalcite: $[Mg_6Al_2(OH)_{16}]CO_3{\cdot}4H_2O$.[103,106] Then, in order to more precisely represent the newly developed members of the LDH family, $[M_{1-x}^{2+}\ M_x^{3+}\ (OH)_2(A^{n-})_{x/n}]^{x+}mH_2O$ was introduced.[107] Divalent metal ions (M^{2+}) generally included Mg^{2+}, Ni^{2+}, Zn^{2+}, Cu^{2+}, *etc.* and trivalent metal ions (M^{3+}) usually included Al^{3+}, Fe^{3+}, Ga^{3+}, *etc.*[94] The common monovalent (M^+) and tetravalent (M^{4+}) metal ions were Li^+ and Ti^{4+}; x denotes the mole fraction of M^{3+} in the metal ions in the range of 0.20–0.33. Interestingly, the radii of the metal ions M^{2+} and M^{3+} in LDHs were similar and the formed cationic plates were balanced by interlayer anions (A^{n-}) which could be both inorganic and organic anions (*e.g.* $C_6H_4(COO)_2^{2-}$, CO_3^{2-}, Cl^-, NO_3^-, SO_4^{2-}) (Fig. 3).[108–117]

This material has been developed and used extensively since its emergence as a material with a particularly versatile structure. Its diverse properties (such as rich reactive sites,[118] large specific surface area,[119,120] basicity,[41,121,122] variable interlayer anions,[42,121,123] structural memory capabilities,[116,124] and so on) allow for a wide range of applications. For instance, He *et al.* constructed a free-standing electrode FeNi-LDH/CoP/carbon cloth (CC) with an open and hierarchical heterostructure for the oxygen evolution reaction (OER), and FeNi-LDH/CoP/CC shows an extremely small Tafel slope of 33.5 mV dec^{-1}, a large TOF of 0.131 s^{-1} at η = 254 mv, and a high stability over ~18.5 h without degradation.[125] Then, Iqbal *et al.* developed an efficient and facile synthetic method for the preparation of a multicomponent CDs/Ag@Mg-Al-Ce-LDH nanocatalyst by using carbon dots (CDs) which can facilitate the electron transfer and migration, as well as stabilize and improve the dispersion of Ag NPs.[109] The large specific surface area and the layered structure composed of cations play an important role in the adsorption of pollutants in water bodies.[113,126,127] And LDHs can also be invoked in other manufacturing applications, such as rubber material modifiers,[128] Eco-friendly coatings,[94] photocatalysts,[129,130] and so on (Fig. 4). Herein, LDHs have been intensively studied as emerging photocatalytic materials for CO_2 reduction, driven by national carbon peaking and carbon neutrality goals.

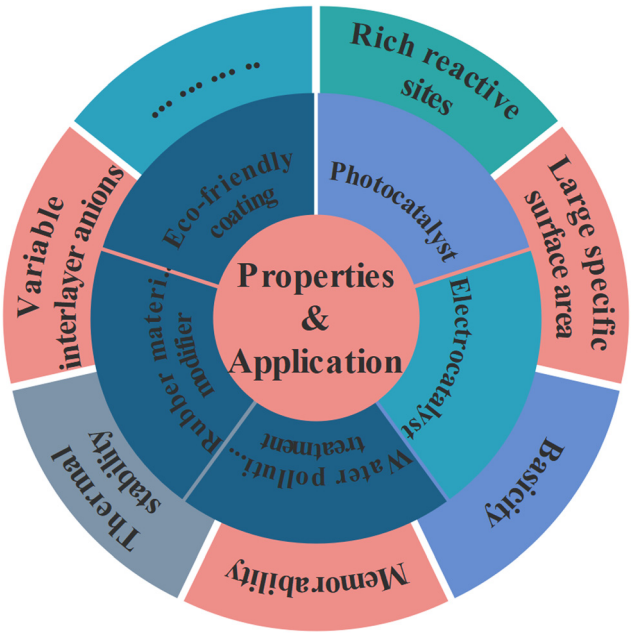

Fig. 4 LDH characteristics and application demonstration.

2.3. Advantages of LDHs for photocatalytic CO_2 reduction

2.3.1. Superior CO_2 adsorption. The two-dimensional layered structure of LDHs provides more active sites and a large specific surface area, which means better adsorption of CO_2 by LDHs during photocatalysis. In recent years, several reports have been published regarding the use of calcined LDHs as CO_2 sorbents in two different temperature ranges. For instance, in $Ti_1Li_3Al_2$-LDHs calcined at different temperatures, the plate structure of the LDHs is distorted to different degrees (Fig. 5a–c).[131] Additionally, as the structure of LDHs begins to distort, the specific surface area of CO_2 gradually increases (Fig. 5f). This increase in surface area, paired with a decrease in the semiconductor band gap of LDHs, promotes the conversion of CO_2 to methane (Fig. 5d and e).

Then, a novel approach where a monolayer of terminal amino groups of APS is grafted onto LDHs (APS/LDHs) for CO_2 capture was explored by Tang *et al.*[70] It was found that the enlarged layer spacing pillared by dodecyl sulfonate is beneficial to APS introduction. APS is tethered to the LDH laminates through covalent interaction. The incorporated amino groups contribute a lot to CO_2 capture on APS/LDHs both through the zwitterion mechanism and weak bonding as confirmed by DRIFTS results. The CO_2 adsorption capacity stabilizes at about 90 mg g^{-1} during the five cycles of adsorption–desorption, showing a great application potential in the temperature swing adsorption processes.

2.3.2. Light adsorption and redox reaction. For most semiconductors, adjusting the bandgap structure typically involves introducing defects or elemental doping, which can be a complex engineering process due to their fixed crystal composition and structure. However, LDH materials offer a unique advantage in that their bandgap structure can be easily adjusted by utilizing tunable ions and morphological structures. This means that the bandgap width, which is closely tied to light absorption and utilization, can be modified without the need for extensive engineering. Similar work has been realized on the photocatalytic CO_2 reduction by ternary LDHs. Kong and co-workers[131] explored the change of light absorption capacity

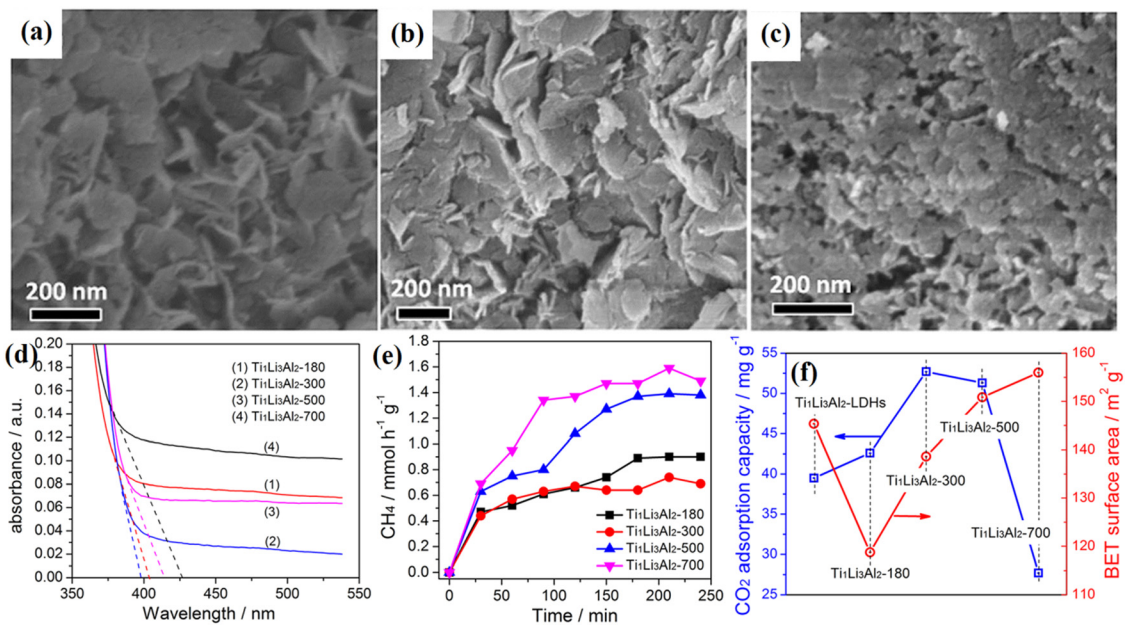

Fig. 5 (a and b) The TEM images of Ti/Li/Al-LDHs under different calcination temperatures, (c) surface area and the CO_2 adsorption capacity of Ti/Li/Al-LDHs calcined at different temperatures, (d) UV-Vis DRS spectra of $Ti1Li_3Al_2$-LDHs calcined at different temperatures, and (e) photocatalytic CH_4 yields of Ti/Li/Al-LDHs calcined at different temperatures, and (f) surface area and the CO_2 adsorption capacity of $Ti1Li_3Al_2$-LDHs calcined at different temperatures (Figures taken with permission from ref. 131 copyright 2023, Nature).

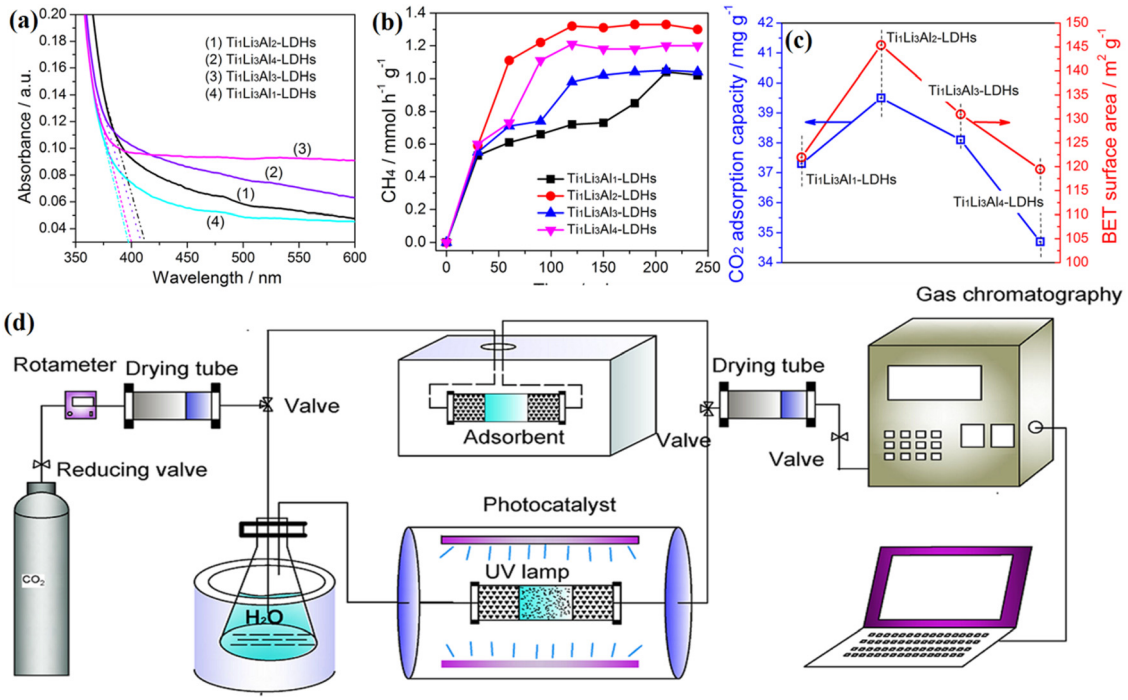

Fig. 6 UV-Vis DRS spectra of (a) Ti/Li/Al-LDHs with different Ti : Li : Al molar ratios. Photocatalytic CH_4 yields of (b) Ti/Li/Al-LDHs with different Ti : Li : Al molar ratios. Surface area and the adsorption capacity of CO_2 for (c) Ti/Li/Al-LDHs with different Ti : Li : Al molar ratios, (d) schematic of the apparatus for CO_2 adsorption and photocatalytic CO_2 reduction (Figures taken with permission from ref. 131 copyright 2023, Nature).

of LDHs without changing the plate structure of LDHs by changing the proportion of Ti : Li : Al elements in the TiLiAl-LDH structure. UV-Vis DRS (Fig. 6a) analysis indicates that all of those Ti/Li/Al-LDHs show outstanding optical absorption under ultraviolet light and the bandgap gradually changes on modifying the proportion of Ti : Li : Al elements. Then, along with the increase of the Ti : Li : Al molar ratio, $Ti_1Li_3Al_2$-LDH exhibited the best surface area and CO_2 adsorption capacity (Fig. 6c), and this phenomenon explains its highest photocatalytic activity under UV irradiation (Fig. 6b and d). This observation indicated that the adsorption capacity for CO_2 should greatly determine the photocatalytic CO_2 reduction activities of these obtained Ti/Li/Al-LDH samples. And the increased specific surface area affected by the different ratios of Ti : Li : Al molar ratios is exposing more active sites.

In addition to the category of atoms have a great modulating effect on the light absorption properties of LDHs, LDHs containing different kinds of metal ions have been achieved. One common approach is to identify precursors containing a certain ion prior to synthesis, while another approach uses ion exchange. Teng Wang employed the ion exchange method cleverly to immerse NiCo-LDH into 3 mM $Fe(NO_3)_3{\cdot}6H_2O$ aqueous solution at room temperature. Product NiCoFe-LDH is successfully synthesized, which provides a convenient idea for the catalytic design of LDHs.[132] Thereby, a detailed band gap structure of LDHs with different kinds of metal ions should be provided, as shown in Fig. 7.[21,104,133] Fortunately, most of the LDH family can be excited in visible light and, from the inverted band position, their reduction capacity meets the

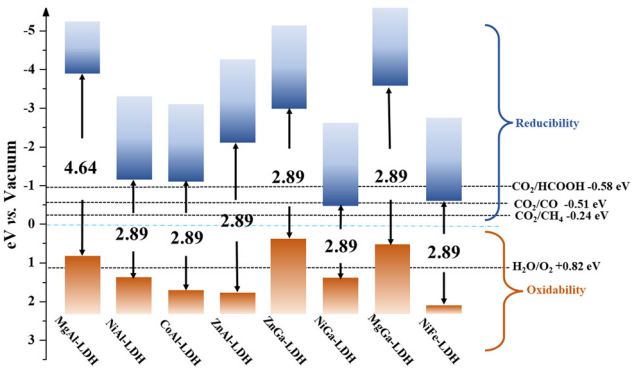

Fig. 7 The band gap structure of common LDH species.

energy required for CO_2 conversion. The flexible synthesis method, adjustable composition, and unique microstructure allow for a wide range of tunability in the conductivity and band gap structure of LDHs. Therefore, the application of LDHs for photocatalytic CO_2 reduction is inevitable.

2.3.3. Separation and migration of photogenerated carriers. Based on the excellent semiconductor properties of LDHs, it is easy to separate photogenerated carriers under illumination conditions. However, it is equally important for the separated photogenerated carriers to migrate to the LDH surface and contact with CO_2. Unfortunately, the conductivity of LDHs is often unsatisfactory and can negatively affect the photocatalytic performance. To address this issue, external interference

Table 2 Variation of the particle size of Mg/Al-CO_3^{2-} LDHs with Mg/Al molar ratios of 2

Molar concentrations of NaOH (M)	Average size (μm)		
	PH 9	PH 10	PH 11
1	2.42	2.57	—
0.5	2.08	2.45	3.1
0.25	1.65	2.43	2.59
0.1	1.97	2.85	2.24

methods such as constructing heterojunctions or loading noble metals can be employed. Size engineering to improve the conductivity of LDHs has been a hot topic in recent years. The common hydrothermal method is not satisfactory for the size modification of LDHs. H S PANDA and his team probed the factors affecting the particle size of LDHs and revealed that PH is the main factor affecting the size of LDHs (Table 2).[134] The micron level size has a limited ability to modulate the electron migration of LDHs. Then, Tokudome *et al.* took a unique approach and a nano-LDH prepared at a high degree of supersaturation has been found to exhibit a high photocatalytic activity towards the reduction of CO_2 in water (Fig. 8).[129] The rate of CO evolution (50 mmol h^{-1}) is 7 times higher than that of the standard LDHs (7.2 mmol h^{-1}), whilst the reaction selectivity towards CO evolution is as high as 80% for the nano-LDH catalyst. The synthesis of small-sized LDH materials has been a challenging task. The most common approach to alter their morphology is through layer exfoliation, which leads to the transformation of blocky LDHs into ultrathin two-dimensional sheets.[23,115,135] The size effect of LDHs is known to promote the rapid migration of electrons on its surface, thereby overcoming the weak conductivity of LDHs. Therefore, the synthesis of LDHs into ultra-small particles of 20 nm size has a significant contribution to the electron migration of the LDH itself, and the application and exploration of this method in the field of photocatalytic reduction of CO_2 still needs further investigation.

In summary, LDHs have a greater potential for development in the field of photocatalysis. This is mainly because the plasticity of their structure drives the favorable enhancement of their photoelectric properties. The unique layered structure provides superior conditions for the uniform distribution of reactive sites. Therefore, studies focusing on structural changes for photocatalytic CO_2 reduction enhancement are pivotal to the application status of LDHs in the field of photocatalysis.

3. Methods for enhancing LDH photocatalytic CO_2 reduction

3.1. Surface modification

3.1.1. Defect engineering. An important structural feature of the LDH materials is that the M^{2+} and M^{3+} cations are distributed in the laminate in a uniform manner, and the diversity and tunability of the lamellar elements make them have a wide range of tunable band gaps. Defect engineering can fine-tune the structure of LDHs and impact their electronic structure.[136] In recent years, defects introduced based on the structural features of LDHs including oxygen vacancies, distortions and doping elements have received extensive attention and discussion. Xiong *et al.*[137] introduced oxygen vacancies to a NiFe-LDH nanoarray using $NaBH_4$ at room temperature in aqueous solution. The HRTEM images and electron diffractions (EDs) of P- and R-NiFe-LDH confirm a slightly destroyed crystal structure caused by the defective nature (Fig. 9a and b). Then, first derivative X-band EPR spectra (Fig. 9c) were carried out to confirm the defect structure of R-NiFe-LDH. While the EPR signal of P-NiFe-LDH is relatively weak (due to the very limited defects), a broad and strong signal of R-NiFe-LDH is detected, demonstrating a defect-rich structure. Moreover, the signals of R-NiFe-LDH at g = 1.99 could be identified as the electrons trapped on oxygen vacancies, indicating that the defects in R-NiFe-LDH are oxygen vacancies. Then, Zhang *et al.*[138] prepared Mn-substituted ZnAl-LDH and found that Mn substitution can effectively promote the surface O vacancy formation. As shown in Fig. 9d, high-resolution TEM (HRTEM) further verifies the high crystallinity. The clear lattice fringes with 0.26 nm correspond to the (101) planes of the LDH structure. And HRTEM reveals that the lattice fringes of MZA have local disorder and dislocation, which indicates that there are a lot of atomic defects on the sample surface. ESR spectra in Fig. 9e clearly display an intense signal (g value of 1.98) on all samples. As this signal features the O vacancy induced local magnetic field, the conclusion is that all the samples exhibited O vacancies. The

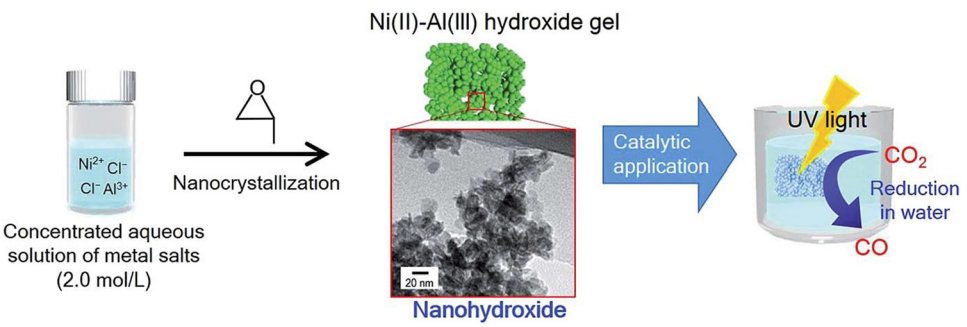

Fig. 8 Schematic illustration of the synthesis and photocatalytic application of the nano-hydroxide and TEM image showing the typical nanostructure of the nano-LDH (Figures taken with permission from ref. 129 copyright 2023, Nature).

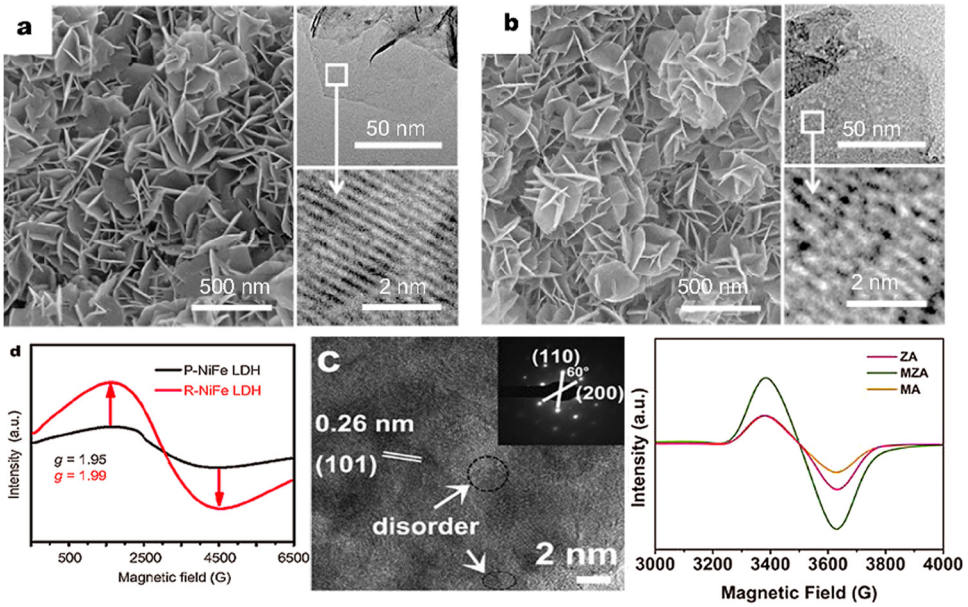

Fig. 9 SEM images of the as-prepared (a) P-NiFe LDH and (b) R-NiFe LDH. The insets are the TEM and HRTEM images of P- and R-NiFe LDH, implying the structure with defects after reduction, (c) EPR characterization of P-NiFe LDH and R-NiFe LDH, (d) HR-TEM image and SAED pattern and (e) ESR spectra of the samples of ZnAl-LDH (Figures taken with permission from ref. 137 and 138 copyright 2023, Springer and Elsevier).

lattice distortion and disorder-defects are caused by defects and also contribute to the photoelectric properties of LDHs.

Fan *et al.* proposed an interlayer anion-mediated CO_2 reduction reaction in LDHs coupled with 5-HMF oxidation. In this subject paper, it was found that stirring the LDHs in potassium hydroxide solution led to an increase in defect density over time (Fig. 10a).[139] These defects were observed to cause subtle changes in the structure of LDHs, which were reflected in the shift of peaks (110) in the XRD pattern (Fig. 10b and c). Also, EPR confirmed the presence of surface defects (Fig. 10d). Defect engineering has a significant impact on the photocatalytic activity of LDH materials due to the formation of electron traps at the defect sites that are favorable for electron aggregation. The vacancies created in the LDH layer can effectively modulate the band gap structure of LDHs, thus increasing their sensitivity to light. As a result of the UV-Vis DRS test in Fig. 11a–d, the defective engineering of the LDHs themselves to make them more suitable for photocatalytic reduction of CO_2 is promising.

3.1.2. Single atom decoration. We have noticed that single-atom catalysis has turned out to be a hot research topic as a unique surface modification tool. The special feature is that single atoms as reaction sites can be fully and uniformly dispersed on the surface of the main catalyst. And single-

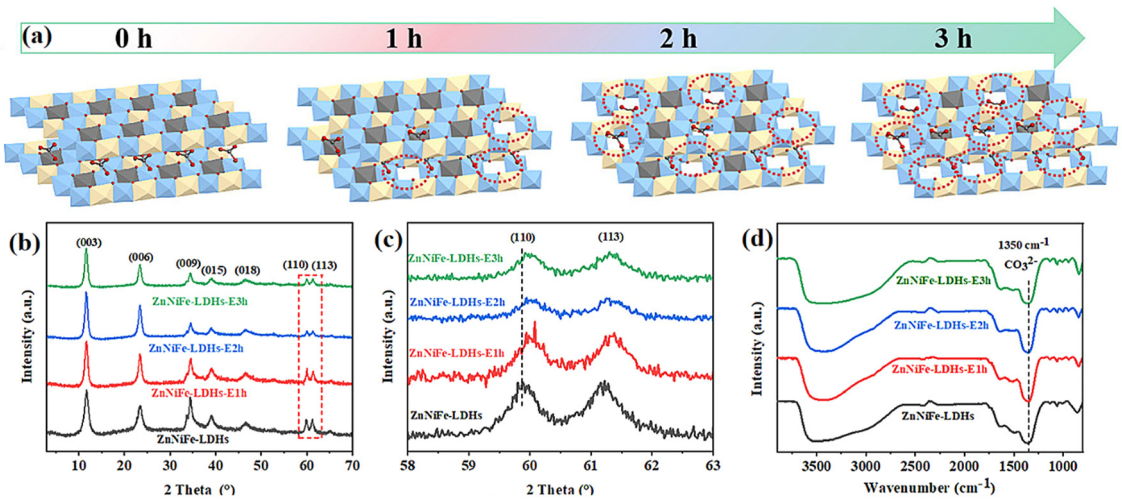

Fig. 10 (a) Scheme of progressive etching of ZnNiFe-LDHs with alkali etching for different periods of time, (b and c) XRD patterns, and (d) EPR spectra (Figures taken with permission from ref. 139 copyright 2023, RSC).

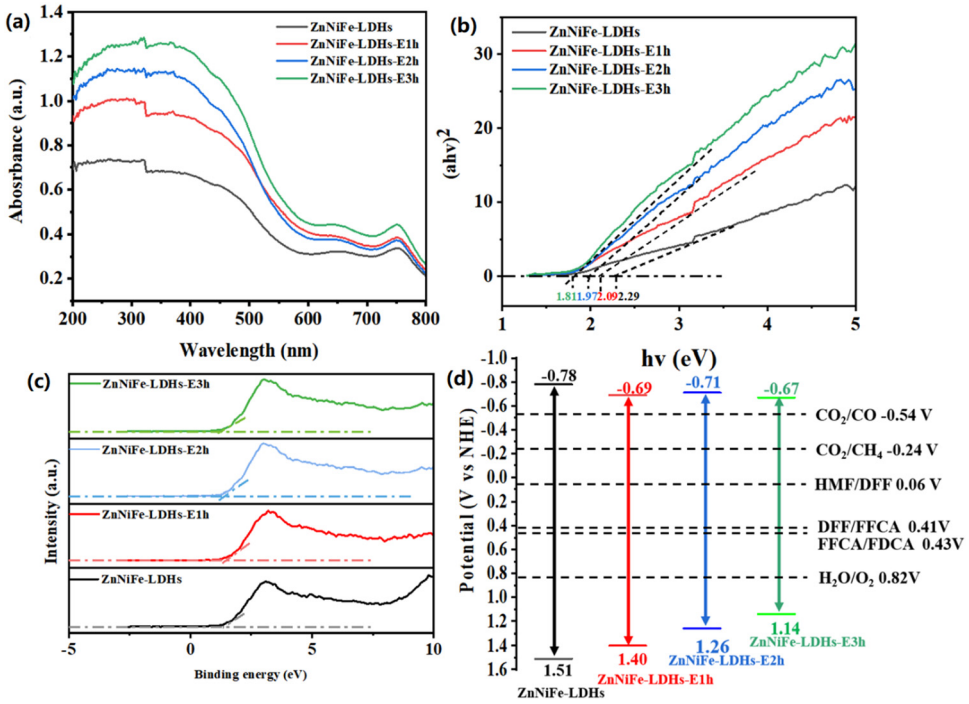

Fig. 11 (a) UV-Vis DRS spectra, (b) energy band gap spectrum, (c) valence band spectrum, and (d) energy band structure of a series of ZnNiFe-LDHs before and after etching (Figures taken with permission from ref. 139 copyright 2023, RSC).

atom photocatalysts have excellent catalytic activity and selectivity in a variety of applications, including sustainable energy conversion, chemical synthesis, CO_2 reduction, environmental remediation, and other areas, owing to their unique electronic structure and high atom usage.[140–142] For instance, Zhang *et al.* firstly employed single-atom Au supported on a NiFe-LDH (Au/NiFe-LDH) catalyst as a model to evaluate the oxygen evolution reaction (OER) activity and understand the activity origin at the atomic level. To confirm the local structure of Au speciation, X-ray absorption near-edge structure (XANES) measurements were performed. The results suggest that Au/NiFe-LDH has a different gold atomic local structural environment compared to that of metallic Au. Moreover, the good accordance of the experimental and simulated results of the Au L_3-edge XANES spectra indicate the presence of single-atom Au and an Au–O bond distance of 1.88 Å. All these results certify the successful formation of Au/NiFe LDH. And the theoretically investigation shows that Au could transfer electrons to LDH, changing the charge distribution and thus further improving the catalytic performance.[143] Kohsuke Mori *et al.* realized an isolated single-atomic Ru catalyst bound on a layered double hydroxide for hydrogenation of CO_2 to formic acid. The authors verified that the anchoring of a Ru precursor onto the surface of LDH in a basic medium successfully generated an isolated single-atomic Ru catalyst surrounded by OH ligands with strong basicity through Ru K-edge FT-EXAFS spectra and the HAADF-STEM image of Ru/LDH. The electronegativity was enhanced by the special location of the hydroxyl groups, which have an ordered arrangement on the LDH surface. Finally, the catalyst achieved the constructive result that under low-pressure conditions, the Ru/LDH catalyst displayed significant catalytic activity for selective CO_2 hydrogenation to produce formic acid due to EMSI and CO_2 concentration effects.[119] LDH materials are recognized as materials with large specific surface area and good compatibility with other materials. Thus, there is a natural advantage of LDHs for the distribution of monoatomic reactive sites. Unfortunately, there is no relevant report to apply the idea of single-atom catalysis to the system of photocatalytic CO_2 reduction by LDH-based photocatalysts.[119,144]

3.2. Element doping

3.2.1. Photoelectric performance. Doping elements into a semiconductor lattice structure can lead to distortion, which in turn promotes defect generation.[145,146] Additionally, exchange ions in LDHs can alter the band gap structure, making elemental doping even more impactful on the photocatalytic CO_2 reduction performance of LDHs. The majority of studies have centered on synthesizing complexes based on LDHs to improve the performance of photocatalytic CO_2 reduction and the adsorption of CO_2 by LDH materials. Therefore, it is crucial to conduct research on the mechanism of elemental doping to understand its impact on the activity of photocatalytic CO_2 reduction and the reaction of LDH materials. A series of Er^{3+} and Er^{3+}/Yb^{3+} doped NiAl-LDH photocatalysts have been successfully fabricated by Xing Hu's team through the solvothermal method. The LDH:1% Er and LDH:1% Er, Y% Yb show strong emissions due to the upconversion effect of Er^{3+}/Yb^{3+}, which can be utilized by LDH for the photocatalytic reduction of CO_2,[147] and the upconversion emission spectra of LDH, LDH:1% Er, and LDH:1% Er, 2% Yb (Fig. 12a). Then, as the

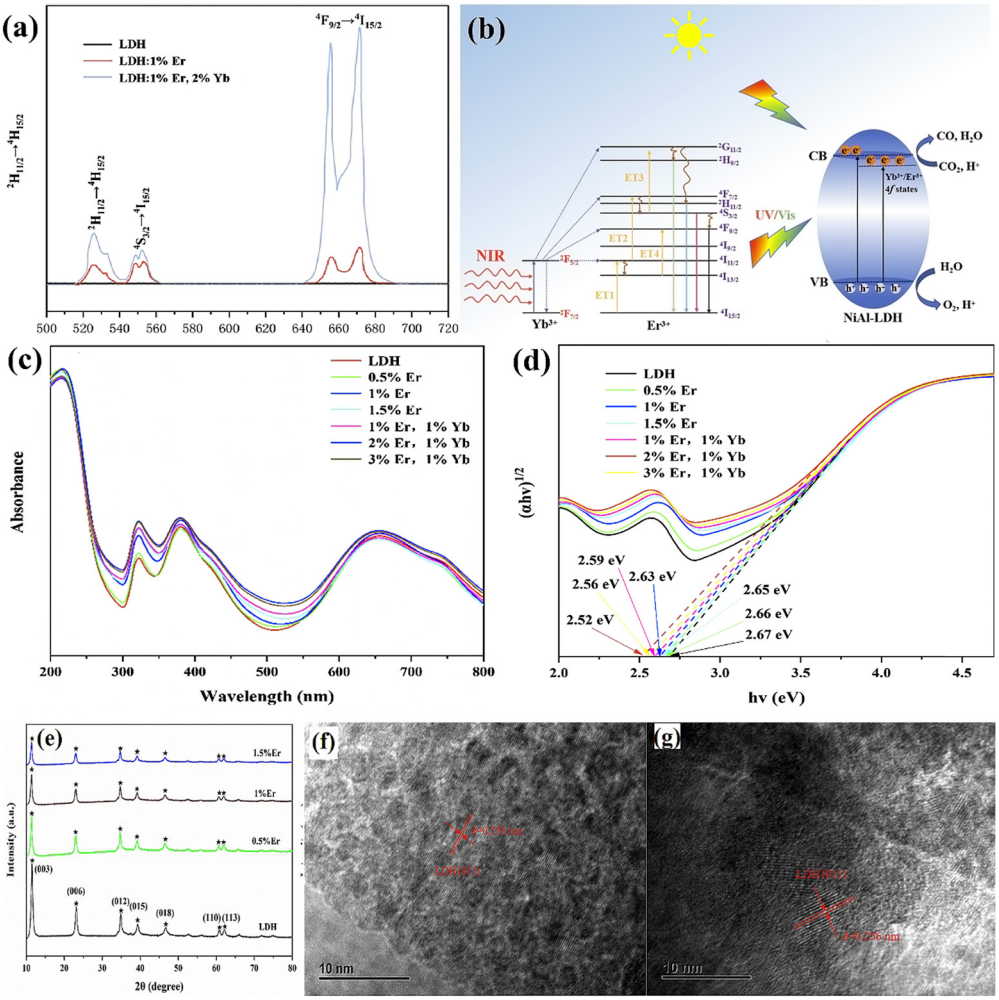

Fig. 12 (a) Upconversion emission spectra of LDH, LDH:1% Er, and LDH:1% Er,2% Yb, (b) schematic diagram of photocatalytic CO_2 reduction under the irradiation of UV-Vis and NIR light, (c) UV-Vis DRS, (d) band-gap energies of the as-prepared samples, (e) XRD patterns of different contents of Er^{3+} doped LDH, (f and g) HRTEM images of pure LDH, LDH:1% Er (Figures taken with permission from ref. 147 copyright 2023, Elsevier).

Er^{3+} and Yb^{3+} content increases, the absorption edges shift to longer wavelengths, which is consistent with the trend of color change and the light absorption capacity of the catalyst is significantly enhanced (Fig. 12b–d). Eventually, the enhanced photocatalytic performance for CO_2 reduction can be attributed to the increased NIR light absorption through the upconversion effect of the co-doped Er^{3+}/Yb^{3+} in the LDH, and the improved photogenerated charge separation efficiency by the Er^{3+}/Yb^{3+} acting as an electron trap. Furthermore, the XRD change curves (Fig. 12e) and lattice spacing (011) (Fig. 12f and g) of the LDHs show that the original lattice spacing becomes smaller, so from the structural point of view, the doping can trigger the distortion of the crystal structure of the LDHs, which is more conducive to the formation of defects. LDHs have a natural advantage in photocatalytic CO_2 reduction, and elemental doping has a gaining effect on the photocatalytic activity of LDHs. Therefore, the adoption of elemental doping to improve the photocatalytic CO_2 reduction performance of LDH materials deserves to be explored in detail.

3.2.2. Density functional theory (DFT) analysis. The doping of transition metals into MgAl-LDH to create surface defects has been considered as an effective strategy to tailor the band gap and promote electron transfer in CO_2 photoreduction.[148] Nevertheless, a report about the comprehensive effect of doped elements in the whole reaction process, especially in CO_2 surface reduction, is still lacking. Herein, Xu *et al.* have investigated the detailed mechanism of doped elements for activity improvement in light absorption, charge transport and surface reaction as revealed by experiments and density functional theory (DFT) calculation.[149] DFT calculation was performed to study the electronic band structures based on Co and Cr doped LDHs. Ten models of LDHs with or without surface defects were considered for DFT calculation, namely MgAl-LDH, MgAl-LDH with one OH vacancy (denoted as MgAl-LDH-V_{OH}), Co-MgAl-LDH, Co-MgAl-LDH with one OH vacancy (Co-MgAl-LDH-V_{OH}), Co-MgAl-LDH with one adjacent OH vacancy (Co-MgAl LDH-V_{OH}-A), Cr-MgAl-LDH, Cr-MgAl-LDH with one OH vacancy (Cr-MgAl LDH-V_{OH}), and Cr-MgAl-LDH

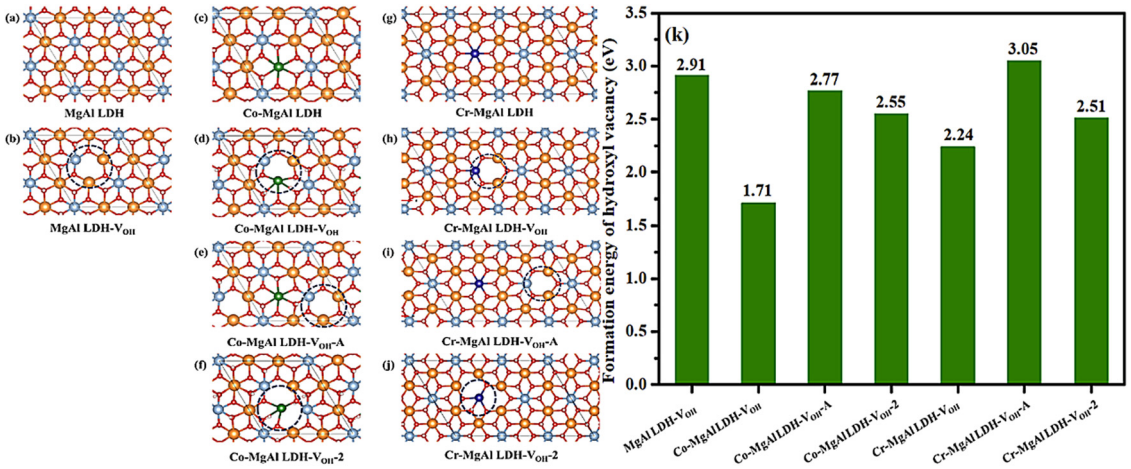

Fig. 13 Optimized structural models of (a) MgAl-LDH, (b) MgAl-LDH with one OH vacancy (MgAl-LDH-V_{OH}), (c) Co-MgAl-LDH, (d) Co-MgAl-LDH with one OH vacancy (Co-MgAl-LDH-V_{OH}), (e) Co-MgAl-LDH with one adjacent OH vacancy (Co-MgAl-LDH-V_{OH}-A), (f) Co-MgAl-LDH with two OH vacancies (Co-MgAl-LDH-V_{OH}-2), (g) Cr-MgAl-LDH, (h) Cr-MgAl-LDH with one OH vacancy (Cr-MgAl-LDH-V_{OH}), (i) Cr-MgAl-LDH with one adjacent OH vacancy (Cr-MgAl- LDH-V_{OH}-A) and (j) Cr-MgAl-LDH with two OH vacancies (Cr-MgAl-LDH-V_{OH}-2) (atoms in different colors: yellow-Mg, light blue-Al, green-Co, blue-Cr, red-O, white-H), (k) Formation energy of the hydroxyl vacancy (V_{OH}) of different defect sites on MgAl-LDH, Co-MgAl-LDH and Cr-MgAl-LDH (Figures taken with permission from ref. 149 copyright 2023, Elsevier).

with one adjacent OH vacancy (Cr-MgAl-LDH-V_{OH}-A). Their optimized structural models are shown in Fig. 13a–i, respectively. From the images of the models, the doping of Co and Cr could nearly introduce distortions to the geometry of MgAl-LDH. Then, the formation of a hydroxyl vacancy (Ef_{OH}) was investigated for the above models with surface defects. As shown in Fig. 13k, the Ef_{OH} values of Co-MgAl-LDH-V_{OH} (1.71 eV) and Cr-MgAl LDH-V_{OH} (2.24 eV) are lower than those of Co-MgAl- LDH-V_{OH}-A (2.77 eV) and Cr-MgAl-LDH-V_{OH}-A (3.05 eV), which confirms that the hydroxyl vacancy near the doped metal site is more favorable than that around the adjacent one-Al-two-Mg region. Therefore, Co-MgAl-LDH-V_{OH} and Cr-MgAl LDH-V_{OH} formation are much easier.

Subsequently, CO_2 surface reaction is also analyzed by DFT calculation based on Co and Cr-doped LDHs. The first step for CO_2 reaction is the adsorption of a CO_2 molecule on the doped metal sites. Around the hydroxyl vacancy of MgAl-LDH-V_{OH}, it may provide two active sites for the adsorption of CO_2 (the Al and the Mg site). At the same time, Cr and Co are directly selected as the potential active sites for the reaction. The optimized structural models of CO_2 adsorption over four metal sites (Fig. 14a–d) and the calculated CO_2 adsorption energies are shown in Fig. 14e. From the images of the adsorption models, the CO_2 molecule is obviously bent and the stable structure is broken after adsorption. For MgAl-LDH-VOH, the adsorption energy of CO_2 is about −2.59 eV on the Al site while the adsorption energy of CO_2 is about −2.47 eV on the Mg site. Therefore, CO_2 prefers to bond to the Al site on MgAl-LDH-V_{OH} and the Mg site will be discarded in the following calculation. The adsorption energies of CO_2 on Co-MgAl-LDH-V_{OH} and Cr-MgAl-LDH-V_{OH} are −2.83 eV and −2.70 eV. It is found that the doped metal could enhance CO_2 adsorption and Co-MgAl-LDH exhibits the advantage of CO_2 adsorption compared with Cr-MgAl LDH. In addition to this, a possible reaction mechanism is suggested in the article (Fig. 14f):

$$CO_2 + * + H^+ + e^- = *CO_2 \quad (1)$$

$$*CO_2 + H^+ + e^- = *COOH \quad (2)$$

$$*COOH + H^+ + e^- = *CO + H_2O \quad (3)$$

$$*CO = * + CO \quad (4)$$

According to the largest free energy change of the electron-involved reaction step, the CO_2 reduction activity trend is that Co-MgAl-LDH-V_{OH} > Cr-MgAl-LDH-V_{OH} > MgAl-LDH-V_{OH}. But in the CO_2 surface reaction, Cr-MgAl-LDH is not optimal in CO_2 adsorption and electrochemical reduction but its advantage lies in the release of CO.

Doping engineering is effective in enhancing the performance of LDHs in photocatalytic reduction of CO_2, but doping with metal ions becomes preferable due to the structure of LDHs. For example, Khan *et al.* induced facile hydrothermal methodology in the synthesis of La incorporated CoAl-LDH nanoplates with different doping ratios, which exhibited promotional performance with the optimum quantity of $Co_2Al_{0.95}La_{0.05}$-LDH.[14] The influence is mainly ascribed to the substitution of Al^{3+} with La^{3+} and the synergistic effect of heterogeneous Co^{2+}/Al^{3+}-La^{3+} with mixed valences. The optimized doping of La resulted in remarkable photocatalytic activity, leading to enhanced production of CO (25.5 μmol g_{cat}^{-1} h^{-1}) and CH_4 (21.80 μmol g_{cat}^{-1} h^{-1}). Compared to pure LDH, more oxygen vacancies and enhanced basicity caused by the addition of La greatly contribute to the photocatalytic CO_2 reduction of $Co_2Al_{0.95}La_{0.05}$-LDH. In addition, similar work has been completed by Deyang Li.[150]

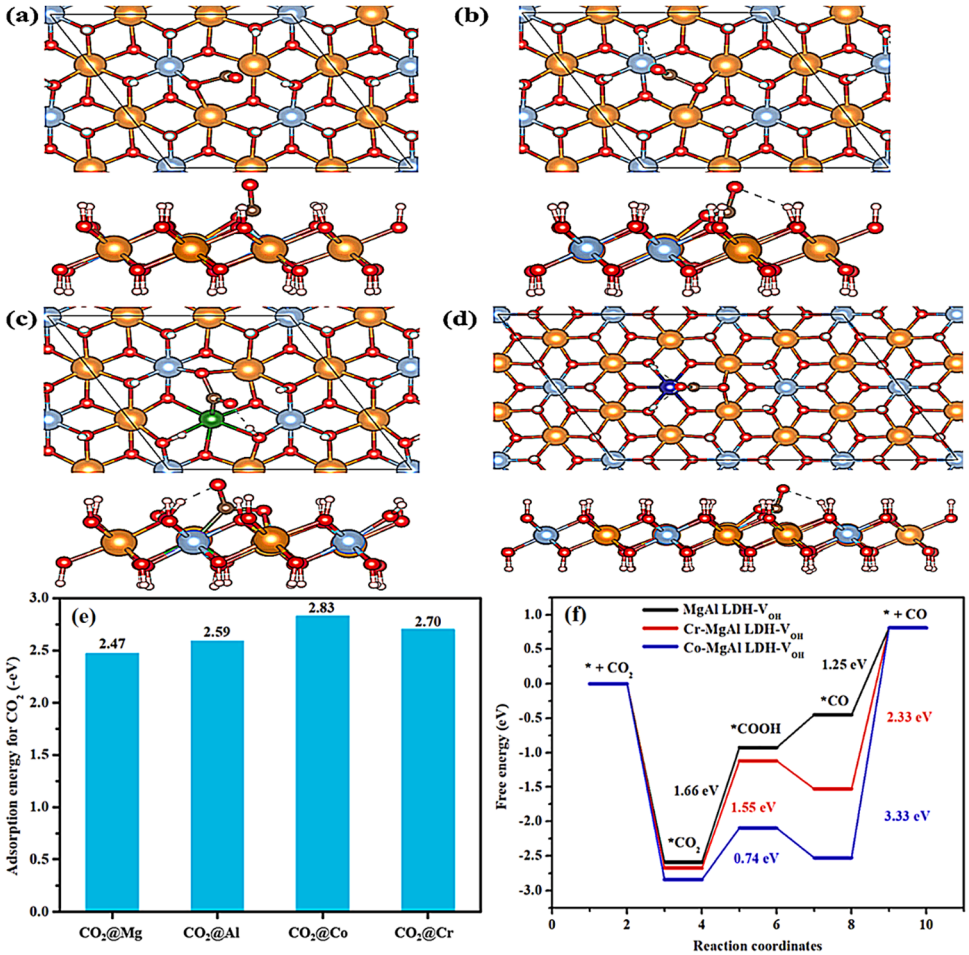

Fig. 14 Optimized structural models of CO_2 adsorption over (a) Mg, (b) Al, (c) Co and (d) Cr sites (Atoms in different colors: yellow-Mg, light blue-Al, green-Co, blue-Cr, red-O, white-H, black-C), (e) CO_2 adsorption energies over different metal sites, and (f) free energy diagram describing the COOH* intermediate from CO_2 to CO over three LDHs (Figures taken with permission from ref. 149 copyright 2023, Elsevier).

The Cu-doped ZnAl-LDHs with a good layer structure are prepared by the coprecipitation method. The doping of Cu^{2+} into the LDH sheets improves the visible light absorption capacity of the ZnAl-LDHs.

3.3. Surface plasma resonance (SPR) effect

Noble metal nanoparticles can greatly promote the photocatalytic reaction, so it is a common method to support noble metals to improve the photocatalytic activity of photocatalysts.[151,152] Interestingly, when the diameter of the loaded noble metal nanoparticles is less than 2 nm, they exhibit semiconductor properties, while the nanoparticles with a diameter greater than 2 nm improve the photocatalytic activity through SPR.[47,91,153–155] Noble metal nanoparticles usually affect photocatalytic activity directly or indirectly. The direct enhancement means that noble metal nanoparticles react directly with catalyzed substances or through contact with active substances such as free radicals. The indirect way is that the noble metal nanoparticles interact with the semiconductor, then, the semiconductor reacts with the reactant.[114,156–158] When the noble metal nanoparticles interact with the semiconductor, the catalytic mechanism is that light irradiation on the photocatalyst causes the noble metal nanoparticles to generate SPR.[159–161] Electrons generated by heat on the metal surface cross the Schottky barrier between the metal nanoparticles and the semiconductor.[161–164] Subsequently, electrons are injected into the CB of the semiconductor, thus increasing the density of photogenerated carriers in the semiconductor and prolonging the residence time of photogenerated carriers on the semiconductor surface, thus promoting the catalysis. Therefore, the conditions of the SPR effect should be followed: I. The wavelength of incident light is close to or less than the radius of the nanoparticles. II. The nanoparticles have the lens effect. III. The photon density on the surface of the precious metal is higher than that on the semiconductor side.[165,166] When the noble metal nanoclusters recombine with semiconductors, e^- and h^+ are usually produced under illumination, and e^- will transfer to the semiconductors or react with the solvents to produce singlet oxygen. This unique photocatalytic gain effect of noble metal nanoparticles can not only act on other semiconductors, but also improve the photocatalytic performance of LDHs. Moreover, LDHs acting as a functional

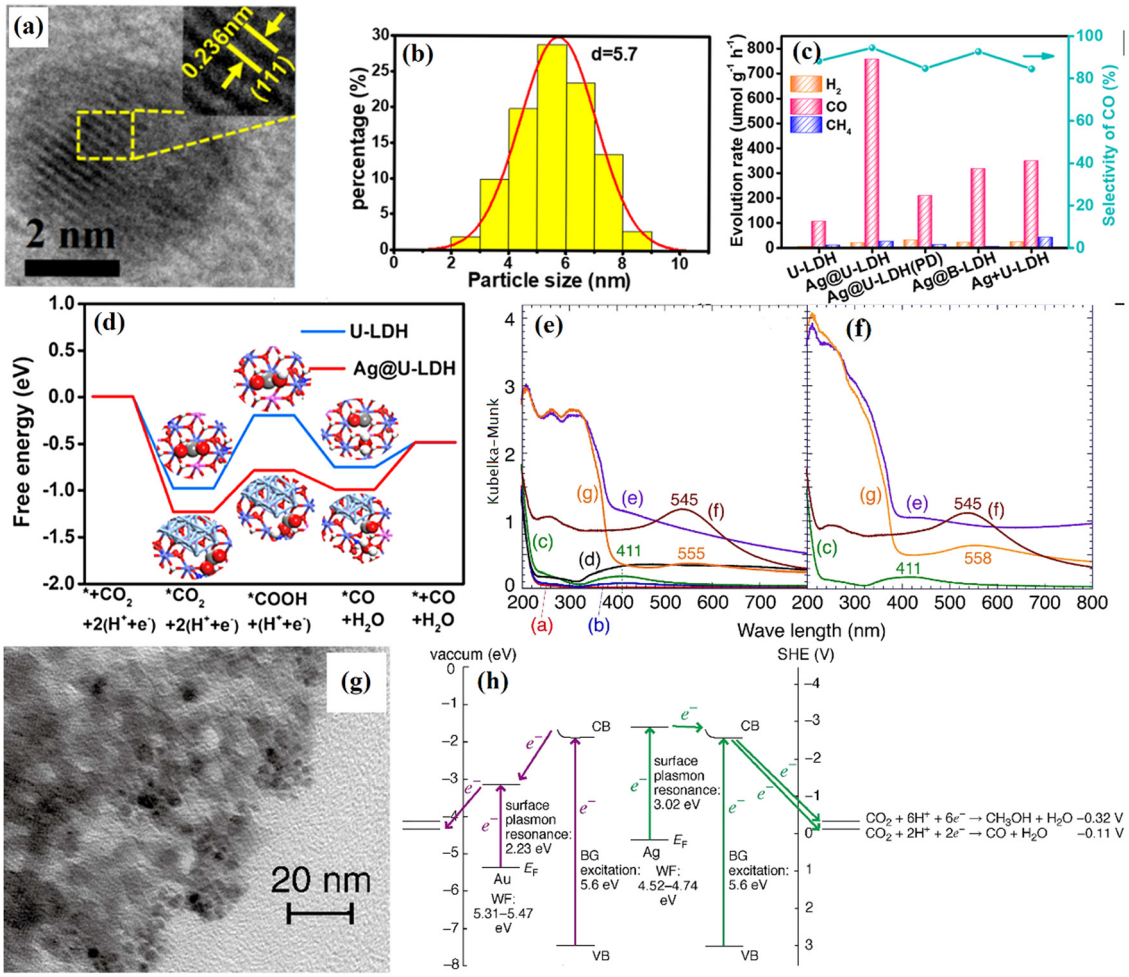

Fig. 15 (a and b) HRTEM image of Ag@U-LDH, lattice photograph, and size of Ag nanoparticles, (c) catalytic evaluation of CO_2 photoreduction under the irradiation of AM 1.5G filter, 100 mW cm^{-2} on the series of catalysts; Ag^+ U-LDH is Ag@U-LDH that is sonicated in water for a certain time, (d) free energy diagrams of CO_2 reduction to CO on U-LDH and Ag@U-LDH (Figures taken with permission from ref. 75 copyright 2023, ACS). (e) UV-Vis DRS spectrum for as-synthesized samples of (a) $Zn_3Ga|CO_3$, (b) Ag/$Zn_3Ga|CO_3$-IE 353-15, (c) Ag/$Zn_3Ga|CO_3$-IE 373-15, (d) Ag/$Zn_3Ga|CO_3$-IE 373-180, (e) Ag/$Zn_3Ga|CO_3$-reconst, (f) Au/$Zn_3Ga|CO_3$-IE, and (g) Au/$Zn_3Ga|CO_3$-reconst, and (f) samples that have been photocatalytically tested for 5 h of (c) Ag/$Zn_3Ga|CO_3$-IE 373-15, (e) Ag/$Zn_3Ga|CO_3$-reconst, (f) Au/$Zn_3Ga|CO_3$-IE, and (g) Au/$Zn_3Ga|CO_3$-reconst, (g) HRTEM image of Au/$Zn_3Ga|CO_3$-reconst, (h) the energy diagram and electron flow in (right) Ag/$Zn_3Ga|CO_3$-IE 373-15 and (left) Au/$Zn_3Ga|CO_3$-reconst during photocatalytic CO_2 reduction (Figures taken with permission from ref. 167 and 168 copyright 2023, Elsevier).

carrier has an unexpected effect on the distribution of such small-sized particles, and it is surprising to prevent the agglomeration of noble metal nanoparticles and cause the uniform distribution of reactive sites.[160]

Zhang and his co-workers reported that Ag@U-LDH acts as a highly efficient photocatalytic CO_2 reduction catalyst.[167] The Ag loaded on the U-LDH surface was identified by HRTEM (Fig. 15a). The supported Ag nanoparticles disperse on U-LDH nanosheets with uniform size. The lattice fringe spacing of Ag is 0.236 nm corresponding to the (111) plane. The size distribution diagram indicates an average Ag nanoparticle size of 5.7 nm with a narrow distribution (Fig. 15b). Therefore, Ag nanoparticles are successfully loaded on the LDH surface and Ag@U-LDH delivers a higher CO evolution rate of 757 μmol g^{-1} h^{-1} than U-LDH (105 μmol g^{-1} h^{-1}) and a high CO selectivity of 94.5% (Fig. 15c). The enhancement mainly stems from the fact that Ag on the surface of LDHs induces a lower formation energy for the *COOH intermediate (Fig. 15d). The conclusion that SPR of precious metals plays a key role in consuming the formation of reactive intermediates on the surface of LDHs is effectively argued. In the study of Shogo Kawamura, the UV absorption characteristics of the LDH photocatalyst with the SPR effect and photocatalytic CO_2 reduction mechanism of the LDH-based photocatalyst loaded with noble metal nanoparticles were investigated and it was found that the SPR effect induces a red-shift in the absorption band when the semiconductor is illuminated, and the light utilization efficiency increases (Fig. 15e and f).[168] An efficient photocatalyst for the conversion of CO_2 into fuel was prepared on the basis of the self-assembly of Ag or Au nanoparticles with $[Zn_3Ga(OH)_8]_2CO_3$-mH_2O layered double hydroxide ($Zn_3Ga|CO_3$ LDH). The TEM of Au/$Zn_3Ga|CO_3$-reconst makes it clear that metal nanoparticles uniformly disperse on the surface of the LDHs (Fig. 15g). The UV-Vis

DRS absorption characteristic peaks of the as-prepared photocatalyst are distributed at 411 and 555 nm attributable to Ag and Au nanoparticles, respectively. And the photocatalytic mechanism with the involvement of SPR is shown in Fig. 15h; the electrons created by SPR of Au are not able to cause photocatalytic CO_2 reduction, whereas E_g electrons in the LDHs excited by UV light are trapped in Au and then transferred to CO_2-derived species. Due to the higher potential of excited state electrons on Au than on the CB of $Zn_3Ga|CO_3$, the oxidation is more favorable for CO formation under UV light.

3.4. Heterojunction

Modification of the internal structure of LDHs has indeed led to significant progress in photocatalytic CO_2 reduction; however, a lower concentration of photogenerated carriers and fast photogenerated carrier recombination are still a great challenge. Therefore, to overcome the common drawback above, researchers have proposed the form of two semiconductors connected, namely a heterojunction. In addition, according to the electron migration paths and structures, heterojunctions have been classified into type-II, all-solid-state indirect heterojunctions and all-solid-state direct heterojunctions.[169,170] Practically, for the photocatalysis of CO_2, heterojunctions can also be considered as excellent candidates due to the enhancement toward optical properties.[122,171–173]

3.4.1. Type-II heterojunctions. The electron migration is significant for the study of the photocatalytic properties of LDH materials.[55,104] In particular, band structure can be calculated through UV-Vis DRS and Mott–Schottky plot measurement. Type-II heterojunctions act as the typical one based on two semiconductors with different bandgap structures built up. A number of researchers have reported the importance of bandgap in LDH-based type-II photocatalysts. For example, Miao *et al.*[74] synthesized a novel ball-flower In_2S_3/NiAl-LDH heterojunction photocatalyst *via* a simple one-step hydrothermal approach for the first time and applied it for CO_2 photocatalytic reduction. The utilization of light is determined by the absorption band and the absorption intensity of the photocatalyst. So, the optical properties of In_2S_3, LDH and In_2S_3/LDH composites are determined by the diffuse reflectance UV-Vis DRS. As shown in Fig. 16a, a slight red shift in the absorption edge is observed in In_2S_3/LDH composites compared with LDH, and with the increase of the In_2S_3 content, the absorption edge shifts towards the longer wavelength region. Then, the band gap energies of In_2S_3, LDH, and 30% In_2S_3/LDH are calculated from DRS spectra by the Kubelka–Munk formula and Tauc plots, which are 2.0, 2.14, and 2.6 eV, respectively (Fig. 16b). In addition, the VB and CB values of In_2S_3 and LDH are determined by the Mott–Schottky method. The flat-band potentials of LDH and In_2S_3 can be obtained by extrapolating to $C^{-2} = 0$ at the frequencies of 500 Hz and 1000 Hz. As shown in Fig. 16c and d, the CB potentials of pure LDH and In_2S_3 are calculated to be −0.56 eV and −0.66 eV, respectively. Whereas, a suitable bandgap structure provides the possibilities for photogenerated carrier migration. However, intimate touch between the semiconductors is a requirement for electron migration between semiconductors.

In addition to the common SEM and TEM, XPS can also reflect the interactions between semiconductors. Zhang *et al.* reported a 3D dahlia-like NiAl-LDH/CdS type-II heterosystem coordinating with a 2D/2D interface, and *in situ* growth of CdS on the surface of the floral spheres of LDHs by a two-step hydrothermal method (Fig. 17a).[124] XPS spectrum is a suitable implement to be used to verify the elemental composition (Ni, Al, Co, S, C and O) of the photocatalyst and the intimate contact between the two semiconductors (Fig. 17b). In view of

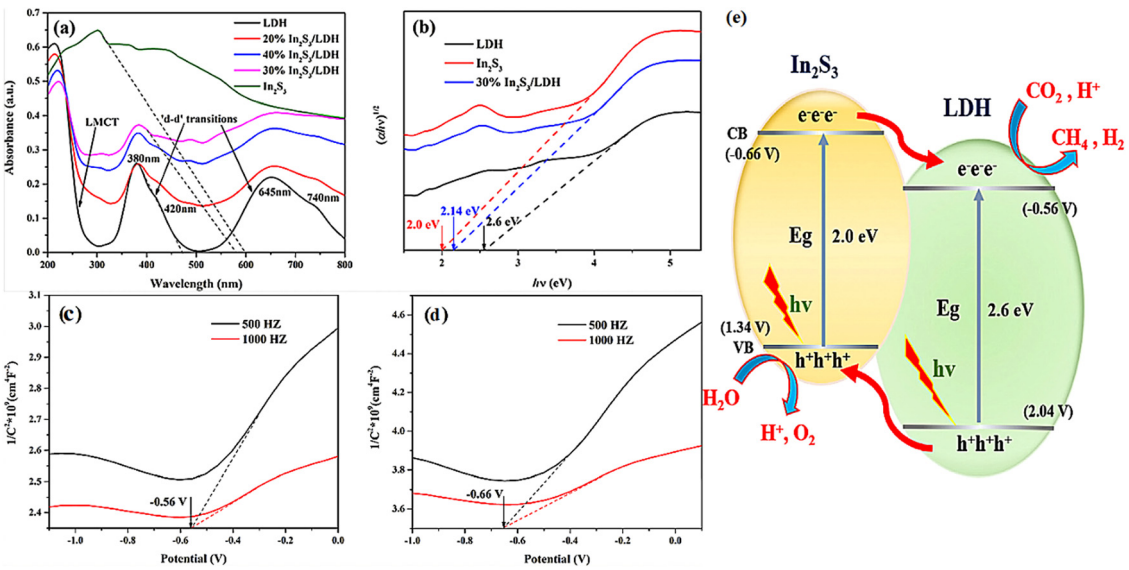

Fig. 16 UV-Vis DRS for pure In_2S_3, pure LDH and In_2S_3/LDH composites (a) and $(\alpha h\nu)_{1/2}$ *versus* energy ($h\nu$) for the band gap energies of pure In_2S_3 and pure LDH (b), Mott–Schottky plots measured for pristine LDH (c) and In_2S_3 and (d and e) CO_2 photoreduction mechanism on the In_2S_3/LDH composites (Figures taken with permission from ref. 74 copyright 2023, ACS).

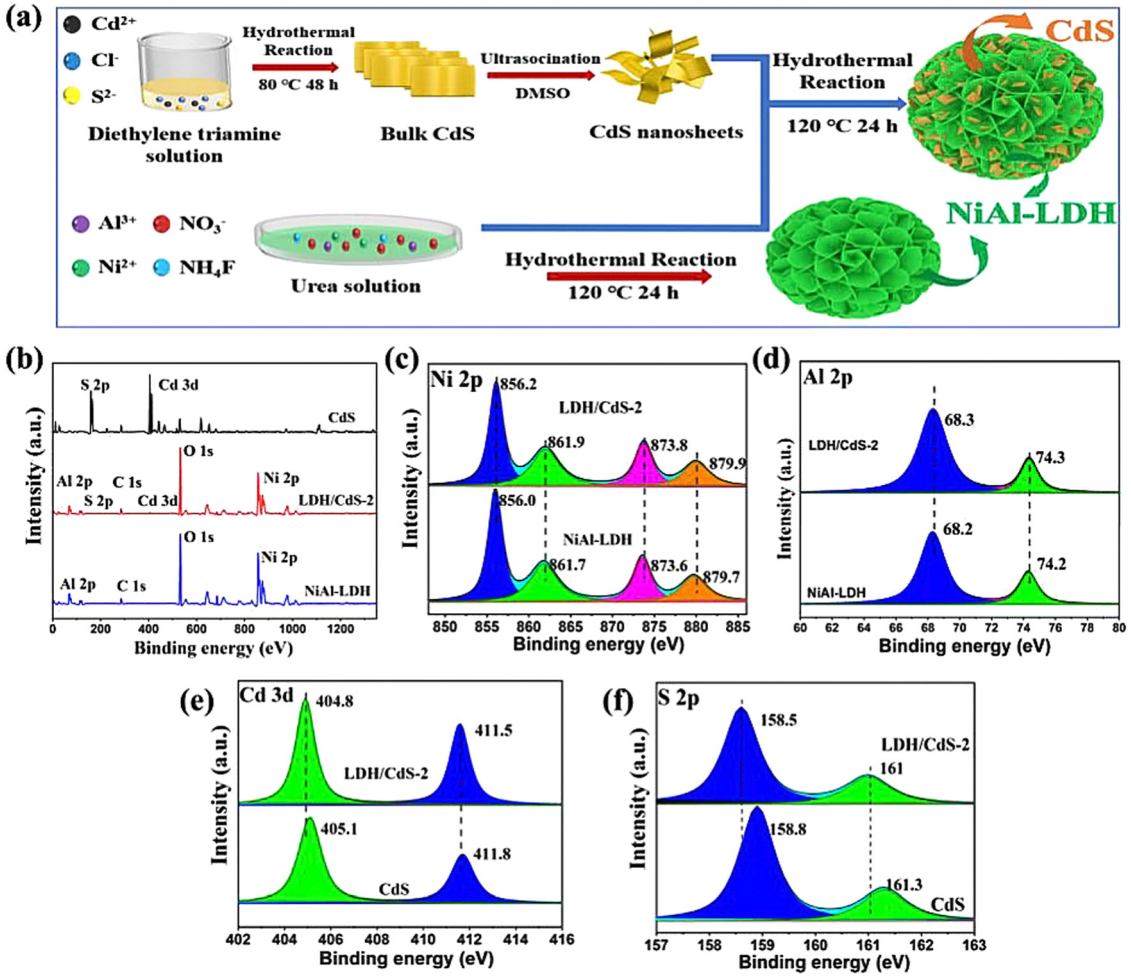

Fig. 17 (a) Illustration of the synthesis of the 3D hierarchical NiAl-LDH/CdS hybrid, (b) XPS survey spectra of NiAl-LDH, CdS and NiAl-LDH/CdS-2, (c) Ni 2p, (d) Al 2p, (e) S 2p, (f) Cd 3d and core-level XPS spectra (Figures taken with permission from ref. 124 copyright 2023, Elsevier).

the high-resolution spectrum results (Fig. 17c–f), the main characteristic peaks of both Ni and Al are red-shifted (reduced binding energy) and those of Cd and S are blue-shifted (increased binding energy), which indicates the interaction between NiAl-LDH and CdS. Moreover, according to the variation of the binding energy for NiAl-LDH and CdS after the integration, the electron migration from NiAl-LDH to CdS can be proposed. The observed change in binding energy implies a possible path of migration for photogenerated carriers, which aligns with the characteristics of a type-II heterojunction. And the 3D hierarchical NiAl-LDH/CdS heterosystem presents 12.45 μmol g^{-1} h^{-1} of CO production (3.3 and 1.6 folds of pristine NiAl-LDH and CdS) with 96% selectivity and superior stability.

The photoelectric properties of two-dimensional lamellar LDHs are exceptional and can be further improved by creating type-II heterojunction photocatalysts with other semiconductors. Additionally, the heterojunction-reinforced structure is more advantageous for the photocorrosion resistance of LDH-based composite photocatalysts (Fig. 18a).[174] The TiO_2/NiAl-LDH core-shell hybrid was obtained *via* a synthesis route involving hydrothermal and calcination treatments but not involving environmentally toxic solvents or surfactants. As shown in Fig. 18b, the result of the steady-state PL spectra means that TiO_2/NiAl-LDH is exposed to light, and it experiences a decrease in the fluorescence effect of photogenerated carriers and a significant improvement in the utilization efficiency of photogenerated carriers. At the same time, the impedance of the composite photocatalyst is reduced (Fig. 18d), which is more favorable for the overall transport of the large number of photogenerated carriers generated during illumination (Fig. 18c). This target TiO_2/LDH core-shell hybrid exhibits the highest CH_4 evolution among the tested samples, with a total yield of 5.14 μmol over 5 h, equating to a rate of 20.56 μmol g^{-1} h^{-1}, representing remarkable 25.7- and 5.0-fold improvements in CH_4 production compared with those of reference TiO_2 NPs and TiO_2 HSs, respectively. Therefore, from the above examples it can be shown that LHD semiconductors can form close contacts with other semiconductors to improve the LDH photoelectrochemical properties and photocatalytic activity.

3.4.2. All-solid-state indirect heterojunction. Z-Scheme heterojunction is the charge transfer method used in the

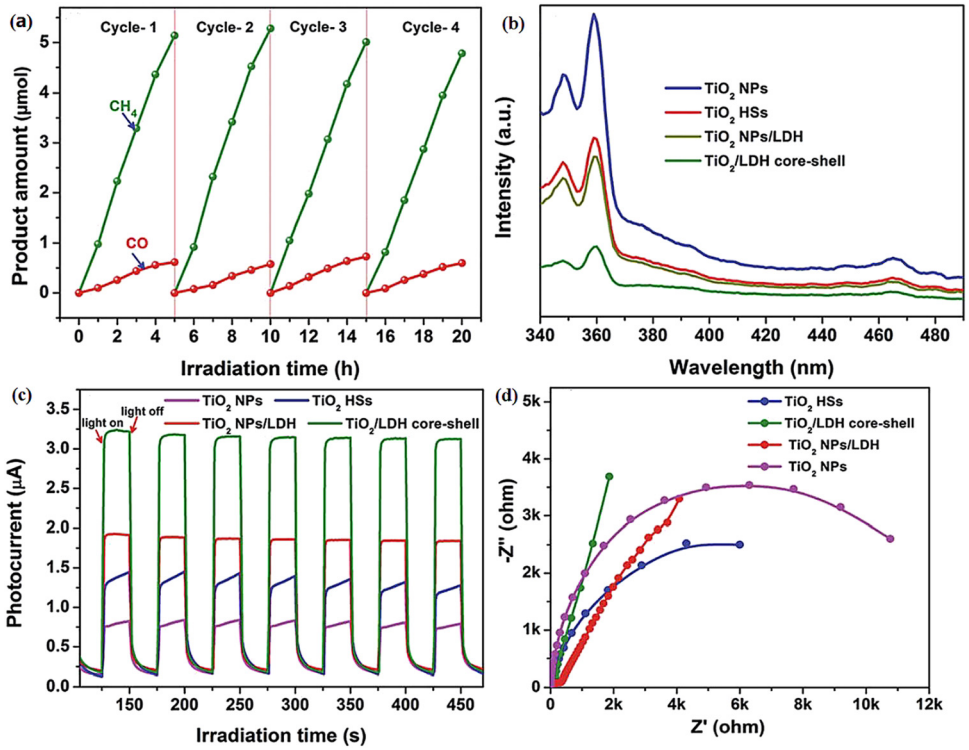

Fig. 18 (a) Recycling tests of CH_4 and CO evolution over the TiO_2/LDH core-shell hybrid, (b) steady-state PL spectra, (c) photocurrent responses, and (d) EIS profiles of the TiO_2 NPs, TiO_2 HSs, TiO_2 NPs/LDH, and TiO_2/LDH core-shell hybrid sample (Figures taken with permission from ref. 174 copyright 2023, RSC).

photoreaction phase of photosynthesis in plants in nature. In order to simulate natural photosynthesis and improve the redox ability of the photocatalysts, Bard proposed the conventional Z-Scheme heterojunction photocatalyst structure in 1979, which is called Z-Scheme because the electron transfer process forms the shape of the letter Z in the diagram.[5,6,175] The commonly used photocatalytic Z-Scheme heterojunction can be divided into all-solid-state direct heterojunctions and all-solid-state indirect heterojunctions whose difference lies in the presence or absence of intermediates. In addition, the strategies of Z-Scheme have long been widely applied in improving the photocatalytic CO_2 reduction activity.[176–178]

For all-solid-state indirect heterojunctions, excellent conductivity mediators present between the host semiconductor and the guest one, include Ag NPs, Au NPs, Pt NPs and graphite.[57,173,179] Compared to liquid-phase media, this approach solves the low dispersion rate of ions that restricts the charge carrier stimulation; however, it causes a shielding effect. Despite such drawbacks, its application for optimizing LDH-based photocatalysts is still effective. It can also show unique advantages over type-II heterojunctions, such as outstanding redox ability. In addition, Z-Scheme heterojunctions show a similar effect to the type-II heterojunctions, including improving the photoelectric properties and catalytic activity of LDH-based photocatalysts. In order to more clearly understand the superiority of Z-Scheme heterojunctions in the field of LDH-based photocatalytic CO_2 reduction and clearly distinguish between Z-Scheme heterojunctions and type-II heterojunctions, a novel Z-Scheme mechanism photocatalyst of Ag-modified α-Fe_2O_3 spherical particles interspersed on hierarchical flower-like NiAl-LDH microspheres (α-Fe_2O_3/Ag/NiAl-LDH, designated as FALDH) was successfully prepared by a combined *in situ* hydrothermal and grafting strategy.[180] Ascribed to the strong interaction between the NiAl-LDH microspheres and the highly-dispersed Ag/α-Fe_2O_3 particles, boosted CO_2 adsorption capacity and optimized bandgap from α-Fe_2O_3, and increased utilization efficiency of light from Ag, the optimal sample of FALDH-5/10 exhibits significantly enhanced photocatalytic activity for CO_2 reduction to CO under simulated sunlight without any sacrificial reagents and photosensitizers. Photocurrent and EIS measurements were carried out to explain the photoelectric superiority of FALDH-5/10, as shown in Fig. 19a and b. And in terms of fluorescence lifetime (Fig. 19c), the heterojunction improves the residence time of photogenerated carriers on the semiconductor surface, thus enhancing the utilization efficiency of photogenerated carriers. For all-solid-state indirect heterojunctions, there is evidence that the structure of semiconductor (I)-mediator-semiconductor (II) plays a crucial role in this system. Chaorong Chen[181] prepared a novel Z-scheme AgBr@Ag/CoAl-LDH photocatalyst, and the Ag NPs are precisely controlled between the two semiconductors, as shown in Fig. 20a and b. Then, one of the main obstacles is that the shielding effect always exists in the Z-Scheme, which is mainly caused by the form of semiconductor (I)-mediator-semiconductor (II).

Then, the significant difference for the migration route of photogenerated carriers that exists in Z-Scheme heterojunctions

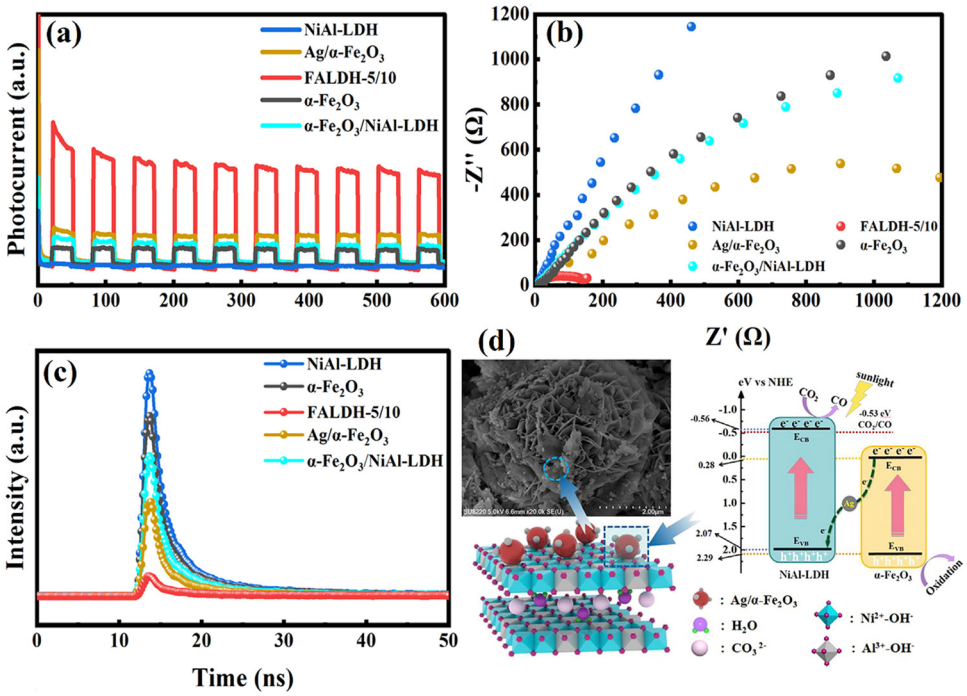

Fig. 19 (a) Photocurrents, (b) EIS spectra, (c) time-resolve fluorescence decay spectra, and (d) the mechanism diagram of FALDH-5/10 (Figures taken with permission from ref. 180 copyright 2023, Elsevier).

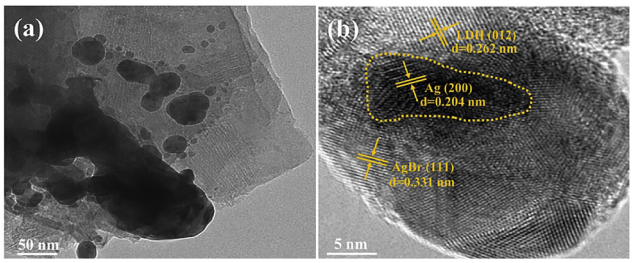

Fig. 20 (a) TEM and (b) HR-TEM of 10% AgBr@Ag/LDH (Figures taken with permission from ref. 181 copyright 2023, Elsevier).

and type-II heterojunctions can be reflected in the ESR spectrum. For example, an enhanced Z-Scheme g-C_3N_4/Ag_3VO_4/rGO heterojunction photocatalyst was successfully prepared by Gao *et al.*[182] for photocatalytic CO_2 reduction and a type-II g-C_3N_4 (CN) foam/LDH heterojunction monolith (NCF) was fabricated through growing NiFe-LDH *in situ* on a porous CN foam substrate by Zhu *et al.*[117] It is obvious from the ESR (Fig. 21a–d) comparison that the Z-Scheme heterojunction releases the full reduction and oxidation capacity of the semiconductor, which is clearly superior to the type-II heterojunction.

3.4.3. All-solid-state direct heterojunction. Compared with indirect heterojunctions connected with intermediate mediators, the omission of the intermediate makes the structure more concise. Two semiconductors linked under the effect of the built-in electric field not only reduce the shielding effect but also improve the economic effect of the photocatalyst. The built-in electric field can be calculated through DFT. Han *et al.*[21] firstly reported a LDH-based Z-scheme heterojunction photocatalyst (NiIn-LDH/In_2S_3) with n-type NiIn-LDH and p-type In_2S_3. The work function (Φ) is calculated to illustrate the electron transfer direction in the NiIn-LDH/In_2S_3 heterojunction. Fig. 22a and b show that the Φ of NiIn-LDH and In_2S_3 are 3.19 and 5.08 eV, thereby the Fermi level (E_F) of NiIn-LDH and In_2S_3 is calculated to be −1.71 and −0.93 eV, respectively. When contacted with each other, the free electrons will flow from NiIn-LDH to In_2S_3 at the interfaces until an equal Fermi level is obtained. Then, density of states (DOS) is calculated to reveal the active site for CO_2 photoreduction. The Ni 3d, O 2p, and S 2p participated in electronic hybridization of CB, while the VB mainly consisted of Ni 3d and In 5p orbitals (Fig. 22c). A suitable bandgap structure is essential for the heterojunction. In addition, a similar bandgap structure to an all-solid-state indirect heterojunction is presented in the all-solid-state direct heterojunction.

Sun *et al.* synthesized a novel $CsPbBr_3$/NiFe-LDH (CPB/LDH) direct Z-Scheme heterojunction photocatalyst using an easy impregnation, then applied it for artificial photocatalytic CO_2 reduction.[111] A suitable band gap structure is necessary for semiconductors to form a direct Z-Scheme heterojunction. UV-Vis DRS spectra of NiFe-LDH and CPB/LDH-*x* (*x* = 1–3), VB-XPS spectra and Tauc plots of CPB and NiFe-LDH show the band gap structures of the semiconductors (Fig. 23a–d). NiFe-LDH as a semiconductor with strong oxidizing properties becomes the oxidizing part of the catalyst, while PBC is mainly responsible for the reduction of CO_2. And from the experimental results, it

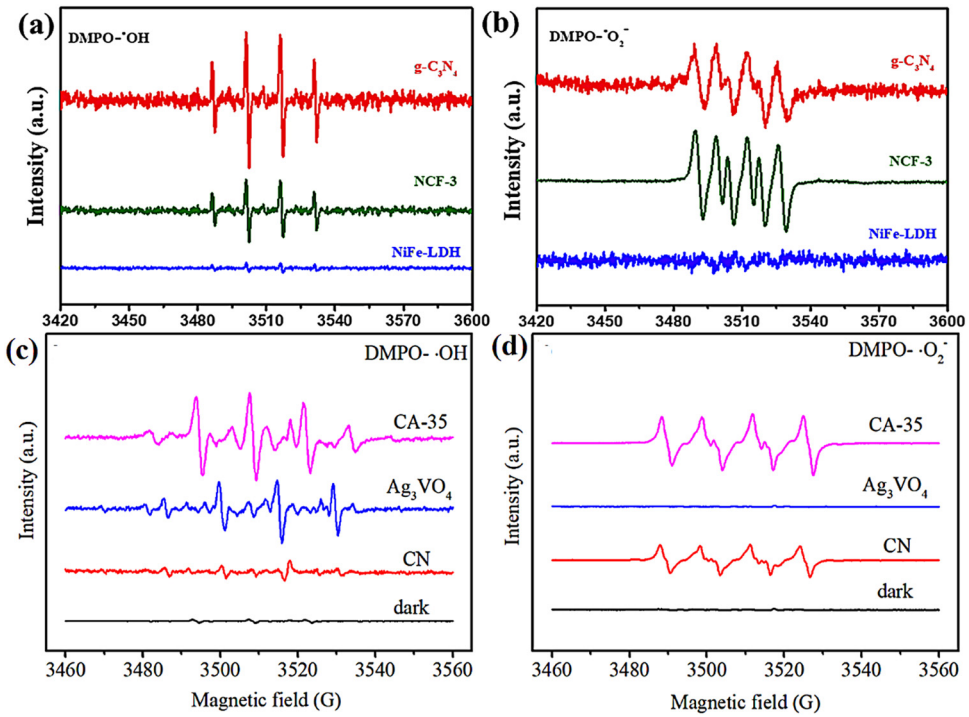

Fig. 21 The ESR spectrum of the type-II g-C_3N_4 foam/LDH photocatalyst (a and b) and Z-Scheme g-C_3N_4/Ag_3VO_4/r-GO photocatalyst (c and d) (Figures taken with permission from ref. 182 and 117 copyright 2023, Elsevier).

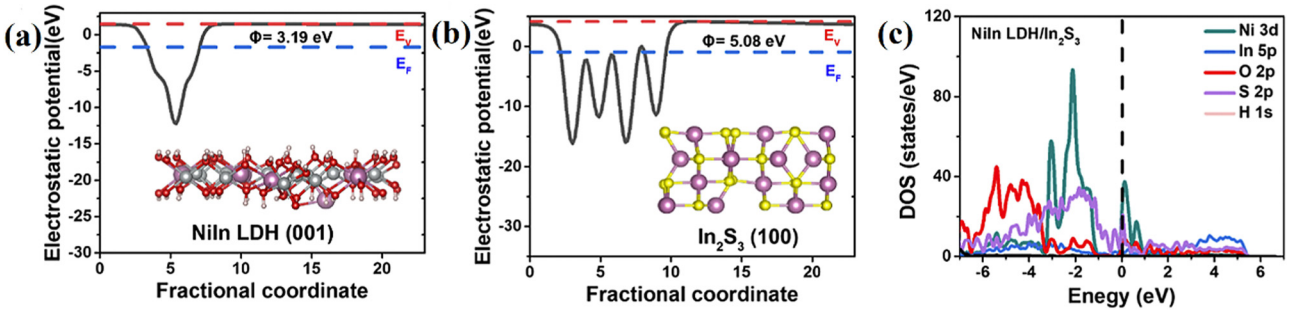

Fig. 22 The electrostatic potentials of (a) NiIn-LDH and (b) In_2S_3, and (c) the DOS of NiIn-LDH/In_2S_3 (Figures taken with permission from ref. 21 copyright 2023, Elsevier).

can be seen that the formation of NiFe-LDH-based heterojunctions improved the adsorption capacity of CO_2, and the level of photocatalytic reduction of CO_2 was substantially increased (product yield rate of pristine NiFe-LDH (7.4 μmol g^{-1} h^{-1}) is comparatively lower than that of the CPB/NiFe-LDH-x (x = 1–3) catalysts). Moreover, the electron consumption rate of CPB/NiFe-LDH-2 (39.58 μmol g^{-1} h^{-1}) is about 2-fold higher than that of pristine NiFe-LDH and CPB, which is counted by Relectrons = 2R(CO) + 8R(CH_4) (Fig. 23f and g). This indicated that by adjusting the content of CPB/NiFe-LDH, the photogenerated carriers in the Z-Scheme can be increased efficiently, which casts controllable Z-Scheme photocatalytic reduction performance. The advantages of the all-solid-state direct heterojunction applied in LDH-based photocatalysts are also obvious: the elimination of the interposer is replaced by a tight coupling between the two semiconductors, which greatly shortens the migration path of the photogenerated carriers and eliminates the cost of the interposer compared to the indirect Z-Scheme heterojunction. Combining the advantages of type-II heterojunctions and indirect Z-Scheme heterojunctions with reduced cost may make it easier to be applied in the field of CO_2 reduction by LDH photocatalysis.

In short, LDH-based catalysts have a bright future for photocatalytic CO_2 reduction applications, and the tunability of their crystal structure allows for better coupling with other semiconductors, resulting in tight junctions. The large specific surface area not only provides sufficient loading sites for the distribution of active sites, but also provides naturally

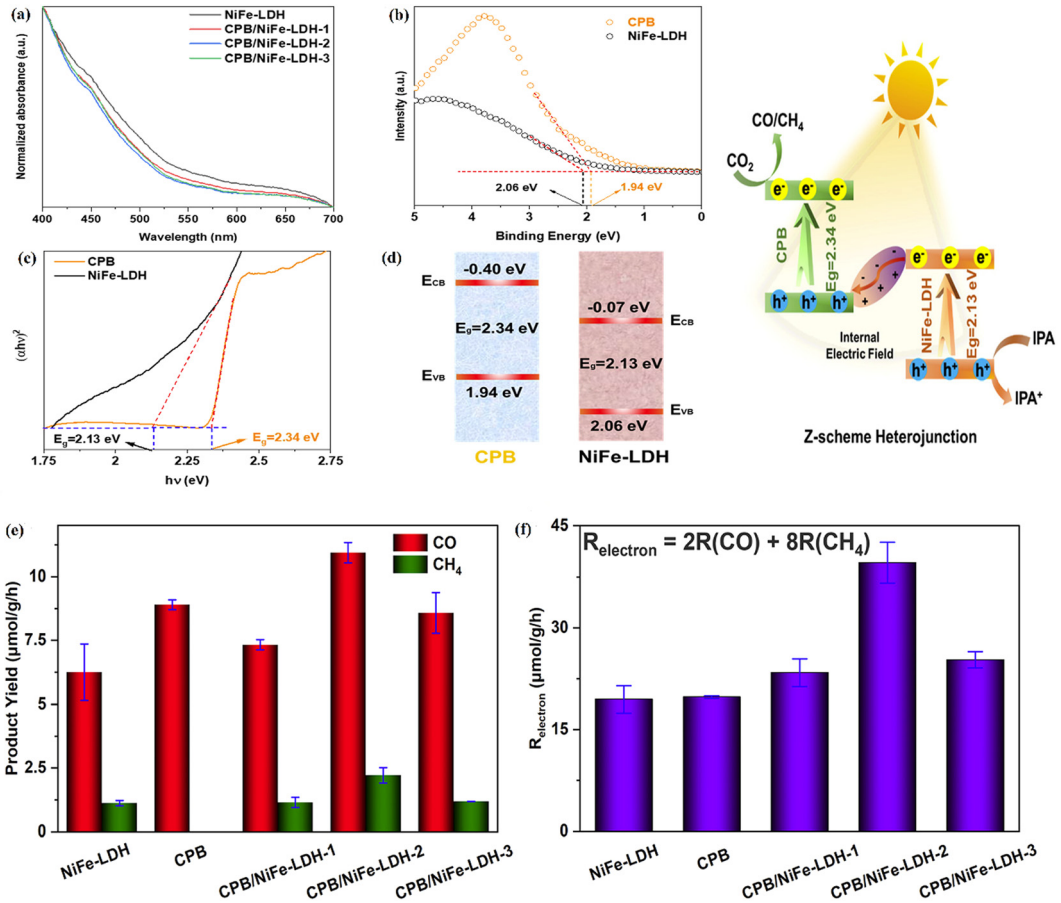

Fig. 23 (a) UV-Vis DRS spectra of NiFe-LDH and CPB/LDH-*x* (*x* = 1–3), (b and c) VB-XPS spectra and Tauc-plots of CPB and NiFe-LDH, (d) energy band alignments of CPB and NiFe-LDH, (e) the product yield rates of the photocatalysts, (f) the electron consumption of pristine NiFe-LDH, CPB and CPB/NiFe-LDH-*x* (*x* = 1–3) (Figures taken with permission from ref. 111 copyright 2023, RSC).

advantageous conditions for CO_2 adsorption. Although their photoelectric properties are weak and their electrical conductivity is not strong, they are well improved by heterojunctions, noble metal loading, and surface engineering. Therefore, the application of LDH materials in photocatalysis is worthy of deeper exploration and development.

Table 3 Summary of the LDH-based photocatalysts for photocatalytic CO_2 reduction

Photocatalysts	Light source	Type	Reducing agent	Products	Performance (μmol g^{-1} h^{-1})	Ref
ZnO	UV-Vis DRS	—	H_2O	CO	0.7	183
Zn_1Al_1-LDH	UV-Vis DRS	—	H_2O	CO	7.6	183
Zn_1Al_2-LDH	UV-Vis DRS	—	H_2O	CO	6.5	183
Zn_1Al_3-LDH	UV-Vis DRS	—	H_2O	CO	0	183
Mg_1Al_1-LDH	UV-Vis DRS	—	Acetonitrile	CO/CH_4	202.2/120.7	184
Ni_3Al_1-LDH	250 W Xe-lamp	—	H_2O	CO	1.63	185
LDH:1% Er, 3% Yb	Visible	Elements doping	H_2O	CO	13.20	147
$NiCo_2O_4$ HCs	Visible	Calcination	2,2-Bipyridine & acetonitrile	CO	10.5	186
$MgCo_2O_4$	Visible	Calcination	2,2-Bipyridine & acetonitrile	CO	6.3	186
Ag/NiAl-LDH	250 W Xe-lamp	Noble metal	H_2O	CO	2.25	185
Pt/ZnCr-LDH	UV	Noble metal	H_2O	CO	7.8	187
Au/ZnCr-LDH	UV	Noble metal	H_2O	CO	3.3	187
Pd/ZnCr-LDH	UV	Noble metal	H_2O	CO	4.6	187
g-C_3N_4/NiAl-LDH	300 W Xe-lamp	Type-II	Nafion solution	CO	8.2	130
NiAl-LDH/CdS	300 W Xe-lamp	Type-II	H_2O	CO	12.45	124
a-Fe_2O_3/Ag/NiAl-LDH	250 W Xe-lamp	Z-Scheme	H_2O	CO	12.7	180
CoZnAl-LDH/RGO/gC_3N_4	300 W Xe-lamp	Z-Scheme	H_2O	CO	10.11	122
CuO/CoAl-LDH	250 W high-pressure Hg-lamp	Z-Scheme	Isopropanol	CO	283.26	188
g-C_3N_4/CoNiFe-LDH	300 W Xe-lamp	Z-Scheme	H_2O	CO	42	116

We also compared these improved solutions for increasing the catalytic activity of LDHs, as shown in Table 3. Pure metal oxides can be used as semiconductor photocatalysts, however the performance in terms of activity in photocatalytic CO_2 reduction is mediocre compared to LDHs containing this metal. And among those methods, heterojunctions for the enhancement of photocatalytic activity are stronger than others. The density and utilization efficiency of photogenerated carriers may play a more important role in the photocatalytic process. Therefore, it is even more important to increase the lifetime of photogenerated carriers in catalysts. In our mind, to achieve the best catalytic effect, the development of modified LDH derivatives as heterojunction photocatalysts would be a wise choice and a favorable direction.

4. Conclusion and outlook

This review comprehensively summarizes recent advances in LDH-based photocatalysts and their application towards photocatalytic CO_2 reduction, and also highlights several main research strategies and potential future directions as shown below.

One of the most important strategies is using LDHs as a precursor to prepare mixed metal oxides or LDOs. The 2D characteristics of the LDHs have an intrinsic high density and uniform distribution of cations within their structures, which reveals a decisive advantage for designing a photocatalyst with a high density of active sites for photocatalytic CO_2 reduction. The use of bimetallic or trimetallic layered hydroxides also has the advantage that the number of active sites can be adjusted by changing the ratio of cations and the type of cationic reaction sites can also have an obvious effect on the photocatalytic reduction of CO_2.

Another important direction focuses on the design of LDH-based nanohybrids. Here, the motivation is to enhance the intrinsically short lifetimes of the LDH charge carriers and promote their extraction. Examples of type-II and Z-Scheme heterojunctions have been reported. Notably, many recent works indicate a dramatic effect of the synthesis method and preparation conditions on the type and morphology of the LDH-based nanohybrids. These affect the structural degree of the materials and, in turn, the electronic interactions between the composite components, thus resulting in synergistic effects.

Other works highlight the role of surface-loaded plasmonic materials in enhancing the catalytic activity of the LDH-based nanohybrids. Noble metal nanoparticles usually affect photocatalytic activity directly or indirectly. Although both the direct path (that means noble metal nanoparticles react directly with catalyzed substances or through contact with active substances) and the indirect route (that the noble metal nanoparticles interact with the semiconductor, then, the semiconductor reacts with the reactant) all can promote the performance of photocatalytic CO_2 reduction, the mechanism still needs to be determined in detail.

Promoting charge carrier separation is also an important function for LDHs that is favorable for the second composite component to increase light absorption and generation of charge carriers. Here, the formation of intimate interfacial contacts in 2D/2D nanocomposites and heterojunctions often yields enhanced charge separation efficiencies. Based on PL, EIS and photocurrent studies, these works further highlight the role and beneficial effect of such a heterojunction. In addition, some of the works also focused on using LDHs as cocatalysts and active catalytic sites and their role in enhancing performance and charge separation efficiency. Due to their compositional and structural characteristics, LDHs can be considered a tunable catalytic platform to address kinetically more complex reactions such as CO_2 reduction. However, some important challenges and insights need to be further discussed and understood, as addressed in the following section:

(i) LDH-derived catalysts and their composite catalysts have shown great potential in the field of photocatalytic CO_2 reduction. However, further studies need to unravel the charge transfer directions of the electrons and holes after charge separation. There are still only a few works that have provided detailed insights into the overall mechanism of photocatalytic CO_2 reduction.

(ii) The synthesis of pristine LDHs and highly crystalline LDH-based materials has always been difficult. The common methods for preparing these materials are co-precipitation, *in situ* growth, self-assembly, and hydrothermal and solvothermal methods, which unfortunately have difficulties in controlling the size distribution and layer thickness of the resulting LDH flakes. Achieving highly active and efficient photocatalytic effects requires an effort to reduce the crystal size and weaken the thickness of the flakes. The exfoliation method has attracted much attention because of its ability to obtain LDHs with ultra-thin and separated layers, high surface area, and extended light-harvesting capability. However, only a few studies have reported their use for photocatalytic CO_2 reduction processes. Future developments on LDH stripping could open new perspectives for other photocatalytic reactions.

(iii) Although there have been significant developments in the catalytic mechanism, synthesis, design and characterisation of photocatalysts developed on the platform of LDHs, there is still a long way to go before they can move from the laboratory to the practical production and commercial level.

In the future, LDHs, an emerging material for photocatalytic CO_2 reduction, will bring a unique opportunity and a great challenge. This review provides meaningful guidance for the rational design and development of LDH-based photocatalysts with high activity, high stability, environmental friendliness and low cost. There is no doubt that there will be a place for LDH-based photocatalysts in the emerging field of photocatalytic reduction of CO_2.

Conflicts of interest

There are no conflicts of interest to declare.

Acknowledgements

This work was supported by the National Natural Science Foundation of China (grant no. 52203110), the Knowledge Innovation Program of Wuhan-Shuguang Project (grant no. 2022010801020216), and the Scientific Research Foundation of Fujian University of Technology (grant no. GY-Z220182).

References

1 Q. Wu, X. Yang, J. Yang, P. Liu, G. Ding, Z. Chen and G. Liao, *J. Colloid Interfance Sci.*, 2023, **644**, 238–245.
2 X. Liu, Y. Zhang, X. Guo and H. Pang, *Adv. Fiber Mater.*, 2022, **4**, 1463–1485.
3 G. Liao, Y. Gong, L. Zhang, H. Gao, G.-J. Yang and B. Fang, *Energy Environ. Sci.*, 2019, **12**, 2080–2147.
4 G. Liao, C. Li, X. Li and B. Fang, *Cell Rep. Phys. Sci.*, 2021, **2**, 100355.
5 G. Liao, C. Li, S.-Y. Liu, B. Fang and H. Yang, *Trends Chem.*, 2022, **4**, 111–127.
6 G. Liao, C. Li, S.-Y. Liu, B. Fang and H. Yang, *Phys. Rep.*, 2022, **983**, 1–41.
7 C. Li, H. Lu, G. Ding, Q. Li and G. Liao, *Catal. Sci. Technol.*, 2023, DOI: **10.1039/D3CY00242J**.
8 R. de_Richter and S. Caillol, *J. Photochem. Photobiol. C: Photochem. Rev.*, 2011, **12**, 1–19.
9 X. Fang, C. Chen, H. Jia, Y. Li, J. Liu, Y. Wang, Y. Song, T. Du and L. Liu, *J. Ind. Eng. Chem.*, 2021, **95**, 16–27.
10 D. Hong, L.-M. Lyu, K. Koga, Y. Shimoyama and Y. Kon, *ACS Sustainable Chem. Eng.*, 2019, **7**, 18955–18964.
11 R. Jia, C. He, Q. Li, S.-Y. Liu and G. Liao, *Trends Biotechnol.*, 2022, **40**, 1425–1438.
12 Z. Yan, G. Liao, X. Zou, M. Zhao, T. Wu, Y. Chen and G. Fang, *J. Agric. Food Chem.*, 2020, **68**, 8341–8349.
13 Z. Yan, B. Song, G. Fang, T. Wu, N. Chen, M. Zhao, X. Zou and G. Liao, *ACS Sustainable Chem. Eng.*, 2021, **9**, 10403–10423.
14 A. Ali Khan and M. Tahir, *Energy Fuels*, 2021, **35**, 8922–8943.
15 B. Fang, Y. Xing, A. Bonakdarpour, S. Zhang and D. P. Wilkinson, *ACS Sustainable Chem. Eng.*, 2015, **3**, 2381–2388.
16 X. Hao, L. Tan, Y. Xu, Z. Wang, X. Wang, S. Bai, C. Ning, J. Zhao, Y. Zhao and Y.-F. Song, *Ind. Eng. Chem. Res.*, 2020, **59**, 3008–3015.
17 S. Liu, L. R. Winter and J. G. Chen, *ACS Catal.*, 2020, **10**, 2855–2871.
18 C. Li, W. Che, S. Y. Liu and G. Liao, *Mater. Today Chem.*, 2023, **29**, 101392.
19 J. Li, H. Huang, W. Xue, K. Sun, X. Song, C. Wu, L. Nie, Y. Li, C. Liu, Y. Pan, H.-L. Jiang, D. Mei and C. Zhong, *Nat. Catal.*, 2021, **4**, 719–729.
20 X. Li, Y. Sun, J. Xu, Y. Shao, J. Wu, X. Xu, Y. Pan, H. Ju, J. Zhu and Y. Xie, *Nat. Energy*, 2019, **4**, 690–699.
21 X. Han, B. Lu, X. Huang, C. Liu, S. Chen, J. Chen, Z. Zeng, S. Deng and J. Wang, *Appl. Catal., B*, 2022, **316**, 121587.
22 L. Cheng and Y. Ji, *Green Energy Environ.*, 2022, DOI: **10.1016/j.gee.2022.07.006**.
23 Y. Zhao, G. I. N. Waterhouse, G. Chen, X. Xiong, L. Z. Wu, C. H. Tung and T. Zhang, *Chem. Soc. Rev.*, 2019, **48**, 1972–2010.
24 C. Li, G. Ding, X. Liu, P. Huo, Y. Yan, Y. Yan and G. Liao, *Chem. Eng. J.*, 2022, **435**, 134740.
25 C. Li, X. Liu, G. Ding, P. Huo, Y. Yan, Y. Yan and G. Liao, *Inorg. Chem.*, 2022, **61**, 4681–4689.
26 C. Li, X. Liu, P. Huo, Y. Yan, G. Liao, G. Ding and C. Liu, *Small*, 2021, **17**, 2102539.
27 C. Li, Y. Zhao, X. Liu, P. Huo, Y. Yan, L. Wang, G. Liao and C. Liu, *J. Colloid Interface Sci.*, 2021, **600**, 794–803.
28 B. Yang, X. Li, Q. Zhang, X. Yang, J. Wan, G. Liao, J. Zhao, R. Wang, J. Liu, R. D. Rodriguez and X. Jia, *Appl. Catal., B*, 2022, **314**, 121521.
29 Y.-J. Zhang, J.-Z. Cheng, Y.-Q. Xing, Z.-R. Tan, G. Liao and S.-Y. Liu, *Mater. Sci. Semicond. Proc.*, 2023, **161**, 107463.
30 W. Zhao, M. Ding, P. Yang, Q. Wang, K. Zhang, X. Zhan, Y. Yu, Q. Luo, S. Gao, J. Yang and Y. Xie, *EES Catal.*, 2023, **1**, 36–44.
31 B. Dong, T. Liu, C. Li and F. Zhang, *Chin. Chem. Lett.*, 2018, **29**, 671–680.
32 T. T. Duong, Q. D. Nguyen, S. K. Hong, D. Kim, S. G. Yoon and T. H. Pham, *Adv. Mater.*, 2011, **23**, 5557–5562.
33 J.-Z. Cheng, L.-L. Liu, G. Liao, Z.-Q. Shen, Z.-R. Tan, Y.-Q. Xing, X.-X. Li, K. Yang, L. Chen and S.-Y. Liu, *J. Mater. Chem. A*, 2020, **8**, 5890–5899.
34 Z.-R. Tan, Y.-Q. Xing, J.-Z. Cheng, G. Zhang, Z.-Q. Shen, Y.-J. Zhang, G. Liao, L. Chen and S.-Y. Liu, *Chem. Sci.*, 2022, **13**, 1725–1733.
35 B. Yang, J. Han, Q. Zhang, G. Liao, W. Cheng, G. Ge, J. Liu, X. Yang, R. Wang and X. Jia, *Carbon*, 2023, **202**, 348–357.
36 B. Yang, Z. Wang, J. Zhao, X. Sun, R. Wang, G. Liao and X. Jia, *Int. J. Hydrogen Energy*, 2021, **46**, 25436–25447.
37 J. Yu, H. Huang, F. Bian, C. Liang, Y. Xia, J. Zhang, Y. Gan and W. Zhang, *ACS Appl. Energy Mater.*, 2018, **1**, 7213–7219.
38 B. Zhang, X. He, X. Ma, Q. Chen, G. Liu, Y. Zhou, D. Ma, C. Cui, J. Ma and Y. Xin, *Sep. Purif. Technol.*, 2020, **247**, 116932.
39 C. Zhao, L. Liu, G. Rao, H. Zhao, L. Wang, J. Xu and Y. Li, *Catal. Sci. Technol.*, 2015, **5**, 3288–3295.
40 Y. Zhou, S. Yang, D. Fan, J. Reilly, H. Zhang, W. Yao and J. Huang, *ACS Appl. Nano Mater.*, 2019, **2**, 1027–1032.
41 Z.-z Yang, J.-j Wei, G.-m Zeng, H.-q Zhang, X.-f Tan, C. Ma, X.-c Li, Z.-h Li and C. Zhang, *Coordin. Chem. Rev.*, 2019, **386**, 154–182.
42 D. Xu, G. Fu, Z. Li, W. Zhen, H. Wang, M. Liu, J. Sun, J. Zhang and L. Yang, *Molecules*, 2023, **28**, 738.
43 S. Xie, C. Deng, Q. Huang, C. Zhang, C. Chen, J. Zhao and H. Sheng, *Angew. Chem., Int. Ed.*, 2023, **62**, e202216717.
44 G. Liao, X. Tao and B. Fang, *Matter*, 2022, **5**, 377–379.
45 L. Wang, G. Huang, L. Zhang, R. Lian, J. Huang, H. She, C. Liu and Q. Wang, *J. Energy Chem.*, 2022, **64**, 85–92.
46 R. Wang, G. Jiang, Y. Ding, Y. Wang, X. Sun, X. Wang and W. Chen, *ACS Appl. Mater. Interfaces*, 2011, **3**, 4154–4158.

47 Z. Xiong, H. Wang, N. Xu, H. Li, B. Fang, Y. Zhao, J. Zhang and C. Zheng, *Int. J. Hydrogen Energy*, 2015, **40**, 10049–10062.
48 P. Xia, S. Cao, B. Zhu, M. Liu, M. Shi, J. Yu and Y. Zhang, *Angew. Chem., Int. Ed.*, 2020, **59**, 5218–5225.
49 L. Wu, S. Zheng, H. Lin, S. Zhou, A. Mahmoud Idris, J. Wang, S. Li and Z. Li, *J. Colloid Interface Sci.*, 2023, **629**, 233–242.
50 W. Wang, D. Jiang, X. Chen, K. Xie, Y. Jiang and Y. Wang, *Appl. Surf. Sci.*, 2020, **515**, 145982.
51 L. Wang, W. Chen, D. Zhang, Y. Du, R. Amal, S. Qiao, J. Wu and Z. Yin, *Chem. Soc. Rev.*, 2019, **48**, 5310–5349.
52 K. Wang, C. Miao, Y. Liu, L. Cai, W. Jones, J. Fan, D. Li and J. Feng, *Appl. Catal., B*, 2020, **270**, 118878.
53 S. C. Azimi, F. Shirini and A. Pendashteh, *Environ. Sci. Pollut. Res. Int.*, 2021, **28**, 56449–56472.
54 S. Cao, B. Shen, T. Tong, J. Fu and J. Yu, *Adv. Funct. Mater.*, 2018, **28**, 1800136.
55 S. Li, M. Zhang, Z. Feng, Y. Huang, T. Qian, H. Hu, X. Zheng, P. Liu, H. Liu, T. Xing and M. Wu, *Chem. Eng. J.*, 2021, **424**, 130315.
56 Z.-D. Lin, R.-T. Guo, Y. Yuan, X.-Y. Ji, L.-F. Hong and W.-g Pan, *Appl. Surf. Sci.*, 2021, **567**, 150805.
57 X. Wang, S. Li, Y. Ma, H. Yu and J. Yu, *J. Phys. Chem. C*, 2011, **115**, 14648–14655.
58 H. Zhu, S. Cai, G. Liao, Z. F. Gao, X. Min, Y. Huang, S. Jin and F. Xia, *ACS Catal.*, 2021, **11**, 14751–14771.
59 J. W. Wang, L. Jiang, H. H. Huang, Z. Han and G. Ouyang, *Nat. Commun.*, 2021, **12**, 4276.
60 Y. Zhao, X. Jia, G. I. N. Waterhouse, L.-Z. Wu, C.-H. Tung, D. O'Hare and T. Zhang, *Adv. Energy Mater.*, 2016, **6**, 1501974.
61 S. C. Shit, I. Shown, R. Paul, K. H. Chen, J. Mondal and L. C. Chen, *Nanoscale*, 2020, **12**, 23301–23332.
62 S. Sirisomboonchai, S. Li, A. Yoshida, X. Li, C. Samart, A. Abudula and G. Guan, *ACS Sustainable Chem. Eng.*, 2018, **7**, 2327–2334.
63 L. Sun, R. Zhang, Y. Wang and W. Chen, *ACS Appl. Mater. Interfaces*, 2014, **6**, 14819–14826.
64 R. Sun, Y. Wang, Z. Zhang, Y. Qu, Z. Li, B. Li, H. Wu, X. Hua, S. Zhang, F. Zhang and L. Jing, *Chem. Eng. J.*, 2021, **426**, 131266.
65 S. Sun, W. Wang, D. Li, L. Zhang and D. Jiang, *ACS Catal.*, 2014, **4**, 3498–3503.
66 C. Ning, S. Bai, J. Wang, Z. Li, Z. Han, Y. Zhao, D. O'Hare and Y.-F. Song, *Coordin. Chem. Rev.*, 2023, **480**, 215008.
67 C. Li, B. Cheng, H. Lu, G. Ding, Z. Jiang and G. Liao, *Inorg. Chem.*, 2023, **62**, 6843–6850.
68 H. Wang, J. Li, Y. Wan, A. Nazir, X. Song, P. Huo and H. Wang, *Appl. Surf. Sci.*, 2023, **613**, 155989.
69 D. Uner and M. M. Oymak, *Catal. Today*, 2012, **181**, 82–88.
70 N. Tang, T. He, J. Liu, L. Li, H. Shi, W. Cen and Z. Ye, *Nanoscale Res. Lett.*, 2018, **13**, 55.
71 B. Fang, A. Bonakdarpour, K. Reilly, Y. Xing, F. Taghipour and D. P. Wilkinson, *ACS Appl. Mater. Interfaces*, 2014, **6**, 15488–15498.
72 G. Liao, J. Fang, Q. Li, S. Li, Z. Xu and B. Fang, *Nanoscale*, 2019, **11**, 7062–7096.
73 A. Khenifi, Z. Derriche, C. Forano, V. Prevot, C. Mousty, E. Scavetta, B. Ballarin, L. Guadagnini and D. Tonelli, *Anal. Chim. Acta*, 2009, **654**, 97–102.
74 Y.-f Miao, R.-t Guo, J.-w Gu, Y.-z Liu, G.-l Wu, C.-p Duan, X.-d Zhang and W.-g Pan, *Appl. Surf. Sci.*, 2020, **527**, 146792.
75 S. Nayak and K. M. Parida, *Sci. Rep.*, 2019, **9**, 2458.
76 S. Nayak, G. Swain and K. Parida, *ACS Appl. Mater. Interfaces*, 2019, **11**, 20923–20942.
77 D. Wang, Y. Wu, Z. Li, H. Pan, Y. Wang, M. Yang and G. Zhang, *Chem. Eng. J.*, 2021, **424**, 130357.
78 G. Wang, Z. Jin and W. Zhang, *J. Colloid Interface Sci.*, 2020, **577**, 115–126.
79 J. Wang, J. Wang, N. Li, X. Du, J. Ma, C. He and Z. Li, *ACS Appl. Mater. Interfaces*, 2020, **12**, 31477–31485.
80 J. Wang, Z. Wang, P. Qu, Q. Xu, J. Zheng, S. Jia, J. Chen and Z. Zhu, *Int. J. Hydrogen Energy*, 2018, **43**, 7388–7396.
81 L. Wang, P. Jin, J. Huang, H. She and Q. Wang, *ACS Sustainable Chem. Eng.*, 2019, **7**, 15660–15670.
82 T. Wang, S. Wang, Z. Cheng, J. Wei, L. Yang, Z. Zhong, H. Hu, Y. Wang, B. Zhou and P. Li, *Chem. Eng. J.*, 2021, **424**, 130323.
83 W. Tan, Y. Li, W. Jiang, C. Gao and C. Zhuang, *ACS Appl. Energy Mater.*, 2020, **3**, 8048–8054.
84 K. Wada, C. S. K. Ranasinghe, R. Kuriki, A. Yamakata, O. Ishitani and K. Maeda, *ACS Appl. Mater. Interfaces*, 2017, **9**, 23869–23877.
85 S. Wan, F. Qi, W. Jin, X. Guo, H. Liu, J. Zhao, J. Zhang and C. Tang, *J. Alloys Compounds*, 2018, **740**, 901–909.
86 C. Wang, R. L. Thompson, J. Baltrus and C. Matranga, *J. Phys. Chem. Lett.*, 2009, **1**, 48–53.
87 Y. Lu, W. Dong, Z. Chen, A. Pors, Z. Wang and S. I. Bozhevolnyi, *Sci. Rep.*, 2016, **6**, 30650.
88 K. Maeda, K. Ishimaki, Y. Tokunaga, D. Lu and M. Eguchi, *Angew. Chem., Int. Ed.*, 2016, **55**, 8309–8313.
89 W. Gao, W. Liu, Y. Leng, X. Wang, X. Wang, B. Hu, D. Yu, Y. Sang and H. Liu, *Appl. Catal., B*, 2015, **176–177**, 83–90.
90 F. Zhang, J. Zhang, H. Wang, J. Li, H. Liu, X. Jin, X. Wang and G. Zhang, *Chem. Eng. J.*, 2021, **424**, 130004.
91 J. Tian, K. Zhong, X. Zhu, J. Yang, Z. Mo, J. Liu, J. Dai, Y. She, Y. Song, H. Li and H. Xu, *Chem. Eng. J.*, 2023, **451**, 138392.
92 L. Tan, K. Peter, J. Ren, B. Du, X. Hao, Y. Zhao and Y.-F. Song, *Front. Chem. Sci. Eng.*, 2020, **15**, 99–108.
93 X. Yang, J. Cheng, B. Fang, X. Xuan, N. Liu, X. Yang and J. Zhou, *Nanoscale*, 2020, **12**, 18437–18445.
94 G. Mascolo and M. C. Mascolo, *Micropor. Mesopor. Mater.*, 2015, **214**, 246–248.
95 H. Park, H. H. Ou, A. J. Colussi and M. R. Hoffmann, *J. Phys. Chem. A*, 2015, **119**, 4658–4666.
96 R. Qiao, M. Mao, E. Hu, Y. Zhong, J. Ning and Y. Hu, *Inorg. Chem.*, 2015, **54**, 9033–9039.
97 G. Sahara and O. Ishitani, *Inorg. Chem.*, 2015, **54**, 5096–5104.

98 A. K. Samantara, S. Chandra Sahu, A. Ghosh and B. K. Jena, *J. Mater. Chem. A*, 2015, **3**, 16961–16970.
99 Z. Zhang, D. S. Kim, C. Y. Lin, H. Zhang, A. D. Lammer, V. M. Lynch, I. Popov, O. S. Miljanic, E. V. Anslyn and J. L. Sessler, *J. Am. Chem. Soc.*, 2015, **137**, 7769–7774.
100 L. Tan, Z. Wang, Y. Zhao and Y. F. Song, *Chem. – Asian J.*, 2020, **15**, 3380–3389.
101 J. Sheng, Y. He, J. Li, C. Yuan, H. Huang, S. Wang, Y. Sun, Z. Wang and F. Dong, *ACS Nano*, 2020, **14**, 13103–13114.
102 W. Shangguan, Q. Liu, Y. Wang, N. Sun, Y. Liu, R. Zhao, Y. Li, C. Wang and J. Zhao, *Nat. Commun.*, 2022, **13**, 3894.
103 A. Razzaq, S. Ali, M. Asif and S.-I. In, *Catalysts*, 2020, **10**, 1185.
104 J. Ren, S. Ouyang, H. Xu, X. Meng, T. Wang, D. Wang and J. Ye, *Adv. Energy Mater.*, 2017, **7**, 1601657.
105 J. Ran, M. Jaroniec and S. Z. Qiao, *Adv. Mater.*, 2018, **30**, 1704649.
106 Z. Qin, J. Wu, B. Li, T. Su and H. Ji, *Acta Phys. Chim. Sin.*, 2020, **37**, 2005027.
107 S. F. Ng, M. Y. L. Lau and W. J. Ong, *Solar RRL*, 2021, **5**, 2000535.
108 Y.-L. Hu, Z. Wu, X. Zheng, N. Lin, Y. Yang, J. Zuo, D. Sun, C. Jiang, L. Sun, C. Lin and Y. Fu, *J. Alloys Compounds*, 2017, **709**, 42–53.
109 K. Iqbal, A. Iqbal, A. M. Kirillov, C. Shan, W. Liu and Y. Tang, *J. Mater. Chem. A*, 2018, **6**, 4515–4524.
110 M. Sohail, H. Kim and T. W. Kim, *Sci. Rep.*, 2019, **9**, 7584.
111 H. Sun, R. Tang, X. Zhang, S. Zhang, W. Yang, L. Wang, W. Liang, F. Li, R. Zheng and J. Huang, *Catal. Sci. Technol.*, 2023, **13**, 1154–1163.
112 M. Tian, C. Liu, Z. G. Neale, J. Zheng, D. Long and G. Cao, *ACS Appl. Mater. Interfaces*, 2019, **11**, 35977–35986.
113 Z. Wang, P. Fang, P. Kumar, W. Wang, B. Liu and J. Li, *Nanomaterials*, 2019, **9**, 807.
114 Z. Wang, Y. Song, J. Zou, L. Li, Y. Yu and L. Wu, *Catal. Sci. Technol.*, 2018, **8**, 268–275.
115 X. Wu, C. Ci, Y. Du, X. Liu, X. Li and X. Xie, *Mater. Chem. Phys.*, 2018, **211**, 72–78.
116 B. Zhu, Q. Xu, X. Bao, D. Lu, H. Yin, Y. Qin and X.-C. Shen, *Catal. Sci. Technol.*, 2021, **11**, 7727–7739.
117 B. Zhu, Q. Xu, X. Bao, H. Yin, Y. Qin and X.-C. Shen, *Chem. Eng. J.*, 2022, **429**, 132284.
118 Y. Ma, X. Yi, S. Wang, T. Li, B. Tan, C. Chen, T. Majima, E. R. Waclawik, H. Zhu and J. Wang, *Nat. Commun.*, 2022, **13**, 1400.
119 K. Mori, T. Taga and H. Yamashita, *ACS Catal.*, 2017, **7**, 3147–3151.
120 J. Low, B. Cheng and J. Yu, *Appl. Surf. Sci.*, 2017, **392**, 658–686.
121 X. Yan and Z. Jin, *Chem. Eng. J.*, 2021, **420**, 127682.
122 Y. Yang, J. Wu, T. Xiao, Z. Tang, J. Shen, H. Li, Y. Zhou and Z. Zou, *Appl. Catal., B*, 2019, **255**, 117771.
123 X. Xiang, L. Bai and F. Li, *AIChE J.*, 2010, **56**, 2934–2945.
124 X. Zhang, Y. Yang, L. Xiong, T. Wang, Z. Tang, P. Li, N. Yin, A. Sun and J. Shen, *Chin. Chem. Lett.*, 2022, **33**, 2111–2116.
125 K. He, T. Tadesse Tsega, X. Liu, J. Zai, X. H. Li, X. Liu, W. Li, N. Ali and X. Qian, *Angew. Chem., Int. Ed.*, 2019, **58**, 11903–11909.
126 Y. Wang, S. Wang, Y. Wu, Z. Wang, H. Zhang, Z. Cao, J. He, W. Li, Z. Yang, L. Zheng, D. Feng, P. Pan, J. Bi, H. Li, J. Zhao and K. Zhang, *J. Alloys Compounds*, 2021, **851**, 156733.
127 S. Yoshino, K. Sato, Y. Yamaguchi, A. Iwase and A. Kudo, *ACS Appl. Energy Mater.*, 2020, **3**, 10001–10007.
128 Q. Shi, X. Zhang, Y. Yang, J. Huang, X. Fu, T. Wang, X. Liu, A. Sun, J. Ge, J. Shen, Y. Zhou and Z. Liu, *J. Energy Chem.*, 2021, **59**, 9–18.
129 Y. Tokudome, M. Fukui, S. Iguchi, Y. Hasegawa, K. Teramura, T. Tanaka, M. Takemoto, R. Katsura and M. Takahashi, *J. Mater. Chem. A*, 2018, **6**, 9684–9690.
130 S. Tonda, S. Kumar, M. Bhardwaj, P. Yadav and S. Ogale, *ACS Appl. Mater. Interfaces*, 2018, **10**, 2667–2678.
131 T. T. Kong, J. Huang, X. G. Jia, W. Z. Wang and Y. Zhou, *Sci. Rep.*, 2019, **9**, 5659.
132 T. Wang, W. Xu and H. Wang, *Electrochim. Acta*, 2017, **257**, 118–127.
133 X. Guan, S. S. Mao and S. Shen, *ChemNanoMat*, 2021, **7**, 873–880.
134 R. Srivastava, D. Bahadur and H. S. Panda, *Bull. Mater. Sci.*, 2011, **34**, 1599–1604.
135 Y. Zhao, S. Zhang, R. Shi, G. I. N. Waterhouse, J. Tang and T. Zhang, *Mater. Today*, 2020, **34**, 78–91.
136 J. Ashtami, X. Joseph, V. Akhil, S. S. Athira and P. V. Mohanan, *Layered 2D Advanced Materials and Their Allied Applications*, 2020, pp. 249–281, DOI: **10.1002/9781119655190.ch11**.
137 X. Xiong, Z. Cai, D. Zhou, G. Zhang, Q. Zhang, Y. Jia, X. Duan, Q. Xie, S. Lai, T. Xie, Y. Li, X. Sun and X. Duan, *Sci. Chin. Mater.*, 2018, **61**, 939–947.
138 X. Chen, J. Wang, Y. Chai, Z. Zhang and Y. Zhu, *Adv. Mater.*, 2021, **33**, 2007479.
139 J. Fan, Y. Zhao, Q. Wang, M. Gao, X. Li, D. Li and J. Feng, *Dalton Trans.*, 2023, **52**, 1950–1961.
140 G. Liao, L. Zhang, C. Li, S.-Y. Liu, B. Fang and H. Yang, *Matter*, 2022, **5**, 3341–3374.
141 Q. Wu, J. Wang, Z. Wang, Y. Xu, Z. Xing, X. Zhang, Y. Guan, G. Liao and X. Li, *J. Mater. Chem. A*, 2020, **8**, 13685–13693.
142 Z.-H. Xue, D. Luan, H. Zhang and X. W. Lou, *Joule*, 2022, **6**, 92–133.
143 J. Liu, J. Zhang, L. Xi, Y. Yu, N. Chen, S. Sun, W. Wang, K. M. Lange and B. Zhang, *J. Am. Chem. Soc.*, 2018, **140**, 3876–3879.
144 D. Zhang, Y. Li, Y. Li and S. Zhan, *SmartMat*, 2022, **3**, 417–446.
145 Z. Qin, M. Qiu, Q. Zhang, S. Yang, G. Liao, Z. Xiong and Z. Xu, *J. Mater. Chem. B*, 2021, **9**, 8882–8896.
146 H. Zhu, C. Zhang, K. Xie, X. Li and G. J. C. E. J. Liao, *Chem. Eng. J.*, 2023, **453**, 139775.
147 X. Hu, R.-t Guo, Z.-d Lin, Z.-x Bi, X. Chen, J. Wang and W.-g Pan, *J. CO_2 Utilization*, 2022, **62**, 102110.
148 J. Wu, Y. Huang, W. Ye and Y. Li, *Adv. Sci.*, 2017, **4**, 1700194.

149 J. Xu, X. Liu, Z. Zhou, L. Deng, L. Liu and M. Xu, *Chem. Eng. J.*, 2022, **442**, 136148.
150 D. Li, L. Fan, Y. Shen, M. Qi, M. D. R. Ali, D. Liu and S. Li, *J. Nanosci. Nanotechnol.*, 2019, **19**, 1090–1097.
151 Z. Jin and Y. Cao, *Sustainable Energy Fuels*, 2021, **5**, 4690–4700.
152 G. Liao, Y. Gong, L. Zhong, J. Fang, L. Zhang, Z. Xu, H. Gao and B. Fang, *Nano Res.*, 2019, **12**, 2407–2436.
153 X. Ren, Y. Wang, A. Liu, Z. Zhang, Q. Lv and B. Liu, *J. Mater. Chem. A*, 2020, **8**, 24284–24306.
154 D. Spanu, A. Minguzzi, S. Recchia, F. Shahvardanfard, O. Tomanec, R. Zboril, P. Schmuki, P. Ghigna and M. Altomare, *ACS Catal.*, 2020, **10**, 8293–8302.
155 C. Wang, R. Yue, H. Wang, C. Zou, J. Du, F. Jiang, Y. Du, P. Yang and C. Wang, *Int. J. Hydrogen Energy*, 2014, **39**, 5764–5771.
156 D. Wang, Y. Li, B. Yu, H. Li, W. Jiang, X. Deng, Y. Wen, C. Liu and G. Che, *Adv. Powder Technol.*, 2021, **32**, 1653–1662.
157 Y. Wei, X. Li, Y. Zhang, Y. Yan, P. Huo and H. Wang, *Renewable Energy*, 2021, **179**, 756–765.
158 M. Zhang, B. Li, Y. Du, G. Zhou, Y. Tang, Y. Shi, B. Zhang, Z. Xu and Q. Huang, *Chem. Eng. J.*, 2021, **424**, 130356.
159 A. Amirjani and D. F. Haghshenas, *Sens. Actuators, B*, 2018, **273**, 1768–1779.
160 K. H. Leong, B. L. Gan, S. Ibrahim and P. Saravanan, *Appl. Surf. Sci.*, 2014, **319**, 128–135.
161 J. Peng, G. Liu, D. Yuan, S. Feng and T. Zhou, *Talanta*, 2017, **167**, 310–316.
162 X. Ji, L. Ge, C. Liu, Z. Tang, Y. Xiao, W. Chen, Z. Lei, W. Gao, S. Blake, D. De, B. Shi, X. Zeng, N. Kong, X. Zhang and W. Tao, *Nat. Commun.*, 2021, **12**, 1124.
163 S. Tonda and W.-K. Jo, *Catal. Today*, 2018, **315**, 213–222.
164 M. Zhou, J. Li, Z. Ye, C. Ma, H. Wang, P. Huo, W. Shi and Y. Yan, *ACS Appl. Mater. Interfaces*, 2015, **7**, 28231–28243.
165 Q. Zhang, Z. Shi, K. Yin, H. Dong, F. Xu, X. Peng, K. Yu, H. Zhang, C. C. Chen, I. Valov, H. Zheng and L. Sun, *Nano Lett.*, 2018, **18**, 5070–5077.
166 M. Li, L. Shen and M.-Q. Yang, *Trans. Tianjin Univ.*, 2022, **28**, 506–532.
167 T. Zhang, H. Shang, B. Zhang, D. Yan and X. Xiang, *ACS Appl. Mater. Interfaces*, 2021, **13**, 16536–16544.
168 S. Kawamura, M. C. Puscasu, Y. Yoshida, Y. Izumi and G. Carja, *Appl. Catal. A: Gen.*, 2015, **504**, 238–247.
169 C. Li, H. Che, C. Liu, G. Che, P. A. Charpentier, W. Z. Xu, X. Wang and L. Liu, *J. Taiwan Inst. Chem. Eng.*, 2019, **95**, 669–681.
170 C. Li, H. Che, Y. Yan, C. Liu and H. Dong, *Chem. Eng. J.*, 2020, **398**, 125523.
171 X. Li, Z. Yu, L. Shao, H. Zeng, Y. Liu and X. Feng, *J. Hazard. Mater.*, 2020, **386**, 121650.
172 S. Megala, P. Ravi, P. Maadeswaran, M. Navaneethan, M. Sathish and R. Ramesh, *Nanoscale Adv.*, 2021, **3**, 2075–2088.
173 J. Yang, J. Hao, S. Xu, Q. Wang, J. Dai, A. Zhang and X. Pang, *ACS Appl. Mater. Interfaces*, 2019, **11**, 32025–32037.
174 W.-K. Jo, S. Moru and S. Tonda, *J. Mater. Chem. A*, 2020, **8**, 8020–8032.
175 K. Wang, J. Li and G. Zhang, *ACS Appl. Mater. Interfaces*, 2019, **11**, 27686–27696.
176 S. Bao, Z. Wang, J. Zhang and B. Tian, *ACS Appl. Nano Mater.*, 2020, **3**, 8604–8617.
177 Y. Che, B. Lu, Q. Qi, H. Chang, J. Zhai, K. Wang and Z. Liu, *Sci. Rep.*, 2018, **8**, 16504.
178 Y. Zhou, G. Chen, Y. Yu, L. Zhao, J. Sun, F. He and H. Dong, *Appl. Catal., B*, 2016, **183**, 176–184.
179 Z. Xie, Y. Xu, D. Li, L. Chen, S. Meng, D. Jiang and M. Chen, *J. Alloys Compounds*, 2021, **858**, 157668.
180 G. Ding, Z. Liu, Q. Wang, Y. Li, W. Liu and Y. Liu, *J. Colloid Interface Sci.*, 2022, **629**, 193–205.
181 C. Chen, H. Zeng, J. Xiong, S. Xu and D. An, *Appl. Clay Sci.*, 2020, **192**, 105627.
182 M. Gao, L. Sun, C. Ma, X. Li, H. Jiang, D. Shen, H. Wang and P. Huo, *Inorg. Chem.*, 2021, **60**, 1755–1766.
183 Y. Zhao, G. Chen, T. Bian, C. Zhou, G. I. Waterhouse, L. Z. Wu, C. H. Tung, L. J. Smith, D. O'Hare and T. Zhang, *Adv. Mater.*, 2015, **27**, 7824–7831.
184 G. Gao, Z. Zhu, J. Zheng, Z. Liu, Q. Wang and Y. Yan, *J. Colloid Interface Sci.*, 2019, **555**, 1–10.
185 M. Elavarasan, W. Yang, S. Velmurugan, J.-N. Chen, Y.-T. Chang, T. C.-K. Yang and T. Yokoi, *J. CO_2* Utilization, 2022, **56**, 101864.
186 B. Han, J. Song, S. Liang, W. Chen, H. Deng, X. Ou, Y.-J. Xu and Z. Lin, *Appl. Catal., B*, 2020, **260**, 118208.
187 K.-i Katsumata, K. Sakai, K. Ikeda, G. Carja, N. Matsushita and K. Okada, *Mater. Lett.*, 2013, **107**, 138–140.
188 Y. Jiang, J. Guo, X. Li, G. Wu, M. Mu and X. Yin, *Sol. Energy*, 2022, **231**, 705–715.